Detection of polarization in the cosmic microwave background using DASI

J. M. Kovac*†‡, E. M. Leitch§†‡, C. Pryke§†‡‖, J. E. Carlstrom§*†‡‖, N. W. Halverson¶† & W. L. Holzapfel¶†

** Department of Physics; † Center for Astrophysical Research in Antarctica; ‡ Center for Cosmological Physics; § Department of Astronomy & Astrophysics and ‖ Enrico Fermi Institute, University of Chicago, 5640 South Ellis Avenue, Chicago, Illinois 60637, USA*
¶ Department of Physics, University of California at Berkeley, Le Conte Hall, California 94720, USA

The past several years have seen the emergence of a standard cosmological model, in which small temperature differences in the cosmic microwave background (CMB) radiation on angular scales of the order of a degree are understood to arise from acoustic oscillations in the hot plasma of the early Universe, arising from primordial density fluctuations. Within the context of this model, recent measurements of the temperature fluctuations have led to profound conclusions about the origin, evolution and composition of the Universe. Using the measured temperature fluctuations, the theoretical framework predicts the level of polarization of the CMB with essentially no free parameters. Therefore, a measurement of the polarization is a critical test of the theory and thus of the validity of the cosmological parameters derived from the CMB measurements. Here we report the detection of polarization of the CMB with the Degree Angular Scale Interferometer (DASI). The polarization is deteced with high confidence, and its level and spatial distribution are in excellent agreement with the predictions of the standard theory.

The CMB radiation provides a pristine probe of the Universe roughly 14 billion years ago, when the seeds of the complex structures that characterize the Universe today existed only as small density fluctuations in the primordial plasma. As the physics of such a plasma are well understood, detailed measurements of the CMB can provide critical tests of cosmological models and can determine the values of cosmological parameters with high precision. The CMB has accordingly been the focus of intense experimental and theoretical investigations since its discovery nearly 40 years ago[1]. The frequency spectrum of the CMB was well determined by the COBE FIRAS instrument[2,3]. The initial detection of temperature anisotropy was made on large angular scales by the COBE DMR instrument[4] and recently there has been considerable progress in measuring the anisotropy on finer angular scales[5–10].

In the now standard cosmological model (see, for example, ref. 11), the shape of the CMB angular power spectrum directly traces acoustic oscillations of the photon-baryon fluid in the early Universe. As the Universe expanded, it cooled; after roughly 400,000 years, the intensity of the radiation field was no longer sufficient to keep the Universe ionized, and the CMB photons decoupled from the baryons as the first atoms formed. Acoustic oscillations passing through extrema at this epoch are observed in the CMB angular power spectrum as a harmonic series of peaks. Polarization is also a generic feature of these oscillations[12–18], and thus provides a model-independent test of the theoretical framework[19–21]. In addition, detection of polarization can in principle triple the number of observed CMB quantities, enhancing our ability to constrain cosmological parameters.

CMB polarization arises from Thompson scattering by electrons of a radiation field with a local quadrupole moment[22]. In the primordial plasma, the local quadrupole moment is suppressed until decoupling, when the photon mean free path begins to grow. At this time, the largest contribution to the local quadrupole is due to Doppler shifts induced by the velocity field of the plasma[23]. CMB polarization thus directly probes the dynamics at the epoch of decoupling. For a spatial Fourier mode of the acoustic oscillations, the velocities are perpendicular to the wavefronts, leading only to perpendicular or parallel alignment of the resulting polarization, which we define as positive and negative respectively. We refer to these polarization modes as scalar *E*-modes in analogy with electric fields; they have no curl component. Because the level of the polarization depends on velocity, we expect that the peaks in the scalar *E*-mode power spectrum correspond to density modes that are at their highest velocities at decoupling and are thus at minimum amplitude. The location of the harmonic peaks in the scalar *E*-mode power spectrum are therefore expected to be out of phase with the peaks in the temperature (*T*) spectrum[15–17].

In light of the above discussion, it is clear that the CMB temperature and polarization anisotropy should be correlated at some level[24]. For a given multipole, the sign of the *TE* correlation should depend on whether the amplitude of the density mode was increasing or decreasing at the time of decoupling. We therefore expect a change in the sign of the *TE* correlation at maxima in the *T* and the *E* power spectra, which correspond to modes at maximum and minimum amplitude, respectively. The *TE* correlation therefore offers a unique and powerful test of the underlying theoretical framework.

Primordial gravity waves will lead to polarization in the CMB[14,25] with an *E*-mode pattern as for the scalar density perturbations, but will also lead to a curl component, referred to as *B*-mode polarization[26–28]. The *B*-mode component is due to the intrinsic polarization of the gravity waves. In inflationary models, the level of the *B*-mode polarization from gravity waves is set by the fourth power of the inflationary energy scale. While the detection of *B*-mode polarization would provide a critical test of inflation, the signal is likely to be very weak and may have an amplitude that is effectively unobservable[29]. Furthermore, distortions to the scalar *E*-mode polarization by the gravitational lensing of the intervening large scale structure in the Universe will lead to a contaminating *B*-mode polarization signal which will severely complicate the extraction of the polarization signature from gravity waves[30–33]. The possibility, however, of directly probing the Universe at energy scales of order 10^{16} GeV by measuring the gravity-wave induced polarization (see, for example, ref. 34) is a compelling goal for CMB polarization observations.

Prior to the results presented in this paper, only upper limits have been placed on the level of CMB polarization. This is due to the low level of the expected signal, demanding sensitive instruments and careful attention to sources of systematic uncertainty (see ref. 35 for a review of CMB polarization measurements).

The first limit to the degree of polarization of the CMB was set in 1965 by Penzias and Wilson, who stated that the new radiation that

they had discovered was isotropic and unpolarized within the limits of their observations[1]. Over the next 20 years, dedicated polarimeters were used to set much more stringent upper limits on angular scales of order several degrees and larger[36–41]. The current best upper limits for the *E*-mode and *B*-mode polarizations on large angular scales are 10 μK at 95% confidence for the multipole range $2 \leq l \leq 20$, set by the POLAR experiment[42].

On angular scales of the order of one degree, an analysis of data from the Saskatoon experiment[43] set the first upper limit (25 μK at 95% confidence for $l \approx 75$); this limit is also noteworthy in that it was the first limit that was lower than the level of the CMB temperature anisotropy. The current best limit on similar angular scales was set by the PIQUE experiment[44]—a 95% confidence upper limit of 8.4 μK to the *E*-mode signal, assuming no *B*-mode polarization. A preliminary analysis of cosmic background imager (CBI) data[45] indicates an upper limit similar to the PIQUE result, but on somewhat smaller scales. An attempt was also made to search for the *TE* correlation using the PIQUE polarization and Saskatoon temperature data[46].

Polarization measurements have also been pursued on much finer angular scales (of the order of an arcminute), resulting in several upper limits (for example, refs 47 and 48). However, at these angular scales, corresponding to multipoles of about 5,000, the level of the primary CMB anisotropy is strongly damped and secondary effects due to interactions with large-scale structure in the Universe are expected to dominate[11].

In this paper, we report the detection of polarized anisotropy in the CMB radiation with the Degree Angular Scale Interferometer (DASI) located at the National Science Foundation (NSF) Amundsen–Scott South Pole research station. The polarization data were obtained during the 2001 and 2002 austral winter seasons. DASI was previously used to measure the temperature anisotropy from $140 < l < 900$, during the 2000 season. We presented details of the instrument, the measured power spectrum and the resulting cosmological constraints in a series of three papers: refs 49, 6 and 50. Prior to the start of the 2001 season, DASI was modified to allow polarization measurements in all four Stokes parameters over the same l range as the previous measurements. The modifications to the instrument, observational strategy, data calibration and data reduction are discussed in detail in a companion paper in this issue[51].

The measurements reported here were obtained within two 3.4° full-width at half-maximum (FWHM) fields separated by 1 h in right ascension. The fields were selected from the subset of fields observed with DASI in 2000 in which no point sources were detected, and are located in regions of low Galactic synchrotron and dust emission. The temperature angular power spectrum is found to be consistent with previous measurements and its measured frequency spectral index is −0.01 (−0.16 to 0.14 at 68% confidence), where 0 corresponds to a 2.73 K Planck spectrum. Polarization of the CMB is detected at high confidence ($\geq 4.9\sigma$) and its power spectrum is consistent with theoretical predictions, based on the interpretation of CMB anisotropy as arising from primordial scalar adiabatic fluctuations. Specifically, assuming a shape for the power spectrum consistent with previous temperature measurements, the level found for the *E*-mode polarization is 0.80 (0.56 to 1.10 68% confidence interval), where the predicted level given previous temperature data is 0.9 to 1.1. At 95% confidence, an upper limit of 0.59 is set to the level of *B*-mode polarization parameterized with the same shape and normalization as the *E*-mode spectrum. The *TE* correlation of the temperature and *E*-mode polarization is detected at 95% confidence and is also found to be consistent with predictions.

With these results contemporary cosmology has passed a long anticipated and crucial test. If the test had not been passed, the underpinnings of much of what we think we know about the origin and early history of the Universe would have been cast into doubt.

Measuring polarization with DASI

DASI is a compact interferometric array optimized for the measurement of CMB temperature and polarization anisotropy[49,51]. Because they directly sample Fourier components of the sky, interferometers are well suited to measurements of the CMB angular power spectrum. In addition, an interferometer gathers instantaneous two-dimensional information while inherently rejecting large-scale gradients in atmospheric emission. For observations of CMB polarization, interferometers offer several additional features. They can be constructed with small and stable instrumental polarization. Furthermore, linear combinations of the data can be used to construct quantities with essentially pure *E*- and *B*-mode polarization response patterns on a variety of scales. This property of the data greatly facilitates the analysis and interpretation of the observed polarization in the context of cosmological models.

DASI is designed to exploit these advantages in the course of extremely long integrations on selected fields of sky. The 13 horn/lens antennas that comprise the DASI array are compact, axially symmetric, and sealed from the environment, yielding small and extremely stable instrumental polarization. Additional systematic control comes from multiple levels of phase switching and field differencing designed to remove instrumental offsets. The DASI mount is fully steerable in elevation and azimuth with the additional ability to rotate the entire horn array about the faceplate axis. The flexibility of this mount allows us to track any field visible from the South Pole continuously at constant elevation angle, and to observe it in redundant faceplate orientations which allow sensitive tests for residual systematic effects.

Instrumental response and calibration

Each of DASI's 13 receivers may be set to admit either left or right circular polarization. An interferometer measures the correlations between the signals from pairs of receivers, called visibilities; as indicated by equation (4) in the 'Theory covariance matrix' subsection recovery of the full complement of Stokes parameters requires the correlation of all four pairwise combinations of left and right circular polarization states (RR, LL, RL and LR), which we refer to as Stokes states. The co-polar states (RR, LL) are sensitive to the total intensity, while the cross-polar states (RL, LR) measure linear combinations of the Stokes parameters *Q* and *U*.

Each of DASI's analogue correlator channels can accommodate only a single Stokes state, so measurement of the four combinations is achieved via time-multiplexing. The polarizer for each receiver is switched on a 1-h Walsh cycle, with the result that over the full period of the cycle, every pair of receivers spends an equal amount of time in all four Stokes states.

In ref. 51, we detail the calibration of the polarized visibilities for an interferometer. In order to produce the calibrated visibilities as defined in equation (4) below, a complex gain factor which depends on the Stokes state must be applied to each raw visibility. Although the cross-polar gain factors could easily be determined with observations of a bright polarized source, no suitable sources are available, and we therefore derive the full calibration through observations of an unpolarized source. The gains for a given pair of receivers (a baseline) can be decomposed into antenna-based factors, allowing us to construct the cross-polar gains from the antenna-based gain factors derived from the co-polar visibilities. DASI's calibration is based on daily observations of the bright H II region RCW38, which we described at length in ref. 49. We can determine the individual baseline gains for all Stokes states with statistical uncertainties <2% for each daily observation. Systematic gain uncertainties for the complete data set are discussed in the 'Systematic uncertainties' section.

The procedure for deriving the baseline gains from antenna-based terms leaves the cross-polar visibilities multiplied by an undetermined overall phase offset (independent of baseline). This phase offset effectively mixes *Q* and *U*, and must be measured to

obtain a clean separation of CMB power into *E*- and *B*-modes. Calibration of the phase offset requires a source whose polarization angle is known, and we create one by observing RCW38 through polarizing wire grids attached to DASI's 13 receivers. From the wire-grid observations, we can derive the phase offset in each frequency band with an uncertainty of $\lesssim 0.4°$.

As an independent check of this phase offset calibration, the Moon was observed at several epochs during 2001–02. Although the expected amplitude of the polarized signal from the Moon is not well known at these frequencies, the polarization pattern is expected to be radial to high accuracy, and this can be used to determine the cross-polar phase offset independently of the wire grid observations. We show in ref. 51 that these two determinations of the phase offset are in excellent agreement.

On-axis leakage

For ideal polarizers, the cross-polar visibilities are strictly proportional to linear combinations of the Stokes parameters *Q* and *U*. For realistic polarizers, however, imperfect rejection of the unwanted polarization state leads to additional terms in the cross-polar visibilities proportional to the total intensity *I*. These leakage terms are the sum of the complex leakage of the two antennas which form each baseline. During the 2000–01 austral summer, DASI's 13 receivers were retrofitted with multi-element broadband circular polarizers designed to reject the unwanted polarization state to high precision across DASI's 26–36 GHz frequency band. Before installation on the telescope, the polarizers were tuned to minimize these leakages.

At several epochs during 2001–02, the antenna-based leakages were determined with a fractional error of 0.3% from deep observations of the calibrator source RCW38. We show in ref. 51 that antenna-based leakages are $\lesssim 1\%$ (of *I*) at all frequency bands except the highest, for which they approach 2%; this performance is close to the theoretical minimum for our polarizer design. Comparison of the measurements from three epochs separated by many months indicates that the leakages are stable with time.

Given the low level of DASI's leakages, the mixing of power from temperature into polarization in the uncorrected visibilities is expected to be a minor effect at most (see the 'Systematic uncertainties' section). Nonetheless, in the analysis presented in this paper, the cross-polar data have in all cases been corrected to remove this effect using the leakages determined from RCW38.

Off-axis leakage

In addition to on-axis leakage from the polarizers, the feeds will contribute an instrumental polarization that varies across the primary beam. Offset measurements of RCW38 and the Moon indicate that the off-axis instrumental polarization pattern is radial, rising from zero at the beam centre to a maximum of about 0.7% near 3°, and then tapering to zero (see also ref. 51).

With the on-axis polarizer leakage subtracted to $\lesssim 0.3\%$ (see above), this residual leakage, while still quite small compared to the expected level of polarized CMB signal (again, see the 'Systematic uncertainties' section), is the dominant instrumental contribution. Although the visibilities cannot be individually corrected to remove this effect (as for the on-axis leakage), it may be incorporated in the analysis of the CMB data. Using fits to the offset data (see ref. 51 for details), we account for this effect by modelling the contribution of the off-axis leakage to the signal covariance matrix as described in the 'Theory covariance matrix' subsection.

CMB observations and data reduction

Observations

For the observations presented here, two fields separated by 1 h of right ascension, at RA = 23 h 30 min and RA = 00 h 30 min with declination −55°, were tracked continuously. The telescope alternated between the fields every hour, tracking them over precisely the same azimuth range so that any terrestrial signal can be removed by differencing. Each 24-h period included 20 h of CMB observations and 2.3 h of bracketing calibrator observations, with the remaining time spent on skydips and miscellaneous calibration tasks.

The fields were selected from the 32 fields previously observed by DASI for the absence of any detectable point sources (see ref. 49). The locations of the 32 fields were originally selected to lie at high elevation angle and to coincide with low emission in the IRAS 100 μm and 408 MHz maps of the sky[52].

The data presented in this paper were acquired from 10 April to 27 October 2001, and again from 14 February to 11 July 2002. In all, we obtained 162 days of data in 2001, and 109 days in 2002, for a total of 271 days before the cuts described in the next section.

Data cuts

Observations are excluded from the analysis, or cut, if they are considered suspect owing to hardware problems, inadequate calibration, contamination from Moon or Sun signal, poor weather or similar effects. In the 'Data consistency and χ^2 tests' section, we describe consistency statistics that are much more sensitive to these effects than are the actual results of our likelihood analysis, allowing us to be certain that the final results are unaffected by contamination. Here we briefly summarize the principal categories of data cuts; we describe each cut in detail in ref. 51.

In the first category of cuts, we reject visibilities for which monitoring data from the telescope indicate obvious hardware malfunction, or simply non-ideal conditions. These include cryogenics failure, loss of tuning for a receiver, large offsets between real/imaginary multipliers in the correlators, and mechanical glitches in the polarizer stepper motors. All data are rejected for a correlator when it shows evidence for large offsets, or excessive noise. An additional cut, and the only one based on the individual data values, is a $>30\sigma$ outlier cut to reject rare ($\ll 0.1\%$ of the data) hardware glitches. Collectively, these cuts reject about 26% of the data.

In the next category, data are cut on the phase and amplitude stability of the calibrator observations. Naturally, we reject data for which bracketing calibrator observations have been lost due to previous cuts. These cuts reject about 5% of the data.

Cuts are also based on the elevation of the Sun and Moon. Co-polar data are cut whenever the Sun was above the horizon, and cross-polar data whenever the solar elevation exceeded 5°. These cuts reject 8% of the data.

An additional cut, which is demonstrably sensitive to poor weather, is based on the significance of data correlations as discussed in the 'Noise model' subsection. An entire day is cut if the maximum off-diagonal correlation coefficient in the data correlation matrix exceeds 8σ significance, referred to gaussian uncorrelated noise. A total of 22 days are cut by this test in addition to those rejected by the solar and lunar cuts.

Reduction

Data reduction consists of a series of steps to calibrate and reduce the data set to a manageable size for the likelihood analysis. Phase and amplitude calibrations are applied to the data on the basis of the bracketing observations of our primary celestial calibrator, RCW38. The raw 8.4-s integrations are combined over each 1-h observation for each of 6,240 visibilities (78 complex baselines × 10 frequency bands × 4 Stokes states). In all cases, on-axis leakage corrections are applied to the data, and sequential 1-h observations of the two fields in the same 15° azimuth range are differenced to remove any common ground signal, using a normalization $(\text{field1} - \text{field2})/\sqrt{2}$ that preserves the variance of the sky signal. Except in the case where the data set is split for use in the χ^2 consistency tests in the 'χ^2 tests' subsection, observations from different faceplate rotation angles, epochs and azimuth ranges are all combined, as well as the two co-polar Stokes states, LL and RR. The resulting data set has $N \leq 4{,}680$ elements ($6{,}240 \times 3/4 = 4{,}680$,

where the 3/4 results from the combination of LL and RR). We call this the uncompressed data set, and it contains all of the information in our observations of the differenced fields for Stokes parameters *I*, *Q* and *U*.

Data consistency and χ^2 tests

We begin our analysis by arranging the data into a vector, considered to be the sum of actual sky signal and instrumental noise: $\mathbf{\Delta} = \mathbf{s} + \mathbf{n}$. The noise vector $\mathbf{n}$ is hypothesized to be gaussian and random, with zero mean, so that the noise model is completely specified by a known covariance matrix $C_N \equiv \langle \mathbf{n}\mathbf{n}^t \rangle$. Any significant excess variance observed in the data vector $\mathbf{\Delta}$ will be interpreted as signal. In the likelihood analysis of the next section, we characterize the total covariance of the data set $C = C_T(\kappa) + C_N$ in terms of parameters κ that specify the covariance C_T of this sky signal. This is the conventional approach to CMB data analysis, and it is clear that for it to succeed, the assumptions about the noise model and the accuracy of the noise covariance matrix must be thoroughly tested. This is especially true for our data set, for which long integrations have been used to reach unprecedented levels of sensitivity in an attempt to measure the very small signal covariances expected from the polarization of the CMB.

Noise model

The DASI instrument and observing strategy are designed to remove systematic errors through multiple levels of differencing. Slow and fast phase switching as well as field differencing are used to minimize potentially variable systematic offsets that could otherwise contribute a non-thermal component to the noise. The observing strategy also includes Walsh sequencing of the Stokes states, observations over multiple azimuth ranges and faceplate rotation angles, and repeated observations of the same visibilities on the sky throughout the observing run to allow checks for systematic offsets and verification that the sky signal is repeatable. We hypothesize that after the cuts described in the previous section, the noise in the remaining data is gaussian and white, with no noise correlations between different baselines, frequency bands, real/imaginary pairs, or Stokes states. We have carefully tested the noise properties of the data to validate the use of this model.

Noise variance in the combined data vector is estimated by calculating the variance in the 8.4-s integrations over the period of 1 h, before field differencing. To test that this noise estimate is accurate, we compare three different short-timescale noise estimates: calculated from the 8.4-s integrations over the 1-h observations before and after field differencing and from sequential pairs of 8.4-s integrations. We find that all three agree within 0.06% for co-polar data and 0.03% for cross-polar data, averaged over all visibilities after data cuts.

We also compare the noise estimates based on the short-timescale noise to the variance of the 1-h binned visibilities over the entire data set (up to 2,700 1-hour observations, over a period spanning 457 days). The ratio of long-timescale to short-timescale noise variance, averaged over all combined visibilities after data cuts, is 1.003 for the co-polar data and 1.005 for the cross-polar data, remarkably close to unity. Together with the results of the χ^2 consistency tests described in the 'χ^2 tests' subsection, these results demonstrate that the noise is white and integrates down from timescales of a few seconds to thousands of hours. We find that scaling the diagonal noise by 1% makes a negligible difference in the reported likelihood results (see the 'Systematic uncertainties' section).

To test for potential off-diagonal correlations in the noise, we calculate a 6,240 × 6,240 correlation coefficient matrix from the 8.4-s integrations for each day of observations. To increase our sensitivity to correlated noise, we use only data obtained simultaneously for a given pair of data vector elements. Owing to the variable number of 8.4-s integrations *M* used to calculate each off-diagonal element, we assess the significance of the correlation coefficient in units of $\sigma = 1/\sqrt{M-1}$. Our weather cut statistic is the daily maximum off-diagonal correlation coefficient significance (see 'Data cuts' subsection).

We use the mean data correlation coefficient matrix over all days, after weather cuts, to test for significant correlations over the entire data set. We find that 1,864 (0.016%) of the off-diagonal elements exceed a significance of 5.5σ, when about one such event is expected for uncorrelated gaussian noise. The outliers are dominated by correlations between real/imaginary pairs of the same baseline, frequency band, and Stokes state, and between different frequency bands of the same baseline and Stokes state. For the real/imaginary pairs, the maximum correlation coefficient amplitude is 0.14, with an estimated mean amplitude of 0.02; for interband correlations the maximum amplitude and estimated mean are 0.04 and 0.003, respectively. We have tested the inclusion of these correlations in the likelihood analysis and find that they have a negligible impact on the results, see the 'Systematic uncertainties' section.

χ^2 tests

As a simple and sensitive test of data consistency, we construct a χ^2 statistic from various splits and subsets of the visibility data. Splitting the data into two sets of observations that should measure the same sky signal, we form the statistic for both the sum and difference data vectors, $\chi^2 = \mathbf{\Delta}^t C_N^{-1} \mathbf{\Delta}$, where $\mathbf{\Delta} = (\mathbf{\Delta}_1 \pm \mathbf{\Delta}_2)/2$ is the sum or difference data vector, and $C_N = (C_{N1} + C_{N2})/4$ is the corresponding noise covariance matrix. We use the difference data vector, with the common sky signal component subtracted, to test for systematic offsets and mis-estimates of the noise. The sum data vector is used to test for the presence of a sky signal in a straightforward way that is independent of the likelihood analyses that will be used to parameterize and constrain that signal.

We split the data for the difference and sum data vectors in five different ways:

(1) Year—2001 data versus 2002 data;

(2) Epoch—the first half of observations of a given visibility versus the second half;

(3) Azimuth range—east five versus west five observation azimuth ranges;

(4) Faceplate position—observations at a faceplate rotation angle of 0° versus a rotation angle of 60°; and

(5) Stokes state—co-polar observations in which both polarizers are observing left circularly polarized light (LL Stokes state) versus those in which both are observing right circularly polarized light (RR Stokes state).

These splits were done on the combined 2001–02 data set and (except for the first split type) on 2001 and 2002 data sets separately, to test for persistent trends or obvious differences between the years. The faceplate position split is particularly powerful, since the six-fold symmetry of the (u, v) plane coverage allows us to measure a sky signal for a given baseline with a different pair of receivers, different backend hardware, and at a different position on the faceplate with respect to the ground shields, and is therefore sensitive to calibration and other offsets that may depend on these factors. The co-polar split tests the amplitude and phase calibration between polarizer states, and tests for the presence of circularly polarized signal.

For each of these splits, different subsets can be examined: co-polar data only, cross-polar data only (for all except the Stokes state split), various *l*-ranges (as determined by baseline length in units of wavelength), and subsets formed from any of these which isolate modes with the highest expected signal to noise (s/n). In constructing the high s/n subsets, we must assume a particular theoretical signal template in order to define the s/n eigenmode basis[53] appropriate for that subset. For this we use the concordance model defined in the 'Likelihood parameters' subsection, although we find the results are not strongly dependent on the choice of

model. Note that the definitions of which modes are included in the high s/n subsets are made in terms of average theoretical signal, without any reference to the actual data. In Table 1, we present the difference and sum χ^2 values for a representative selection of splits and subsets. In each case we give the degrees of freedom, χ^2 value, and probability to exceed (PTE) this value in the χ^2 cumulative distribution function. For the 296 different split/subset combinations that were examined, the χ^2 values for the difference data appear consistent with noise; among these 296 difference data χ^2 values, there are two with a PTE < 0.01 (the lowest is 0.003), one with a PTE > 0.99, and the rest appear uniformly distributed between this range. There are no apparent trends or outliers among the various subsets or splits.

The high s/n mode subsets are more sensitive to certain classes of systematic effects in the difference data vector and more sensitive to the expected sky signal in the sum data vector, that otherwise may be masked by noise. Also, the number of modes with expected $s/n > 1$ gives an indication of the power of the experiment to constrain the sky signal. The co-polar data, which are sensitive to the temperature signal, have many more high s/n modes than the cross-polar data, which measure polarized radiation. Within the context of the concordance model used to generate the s/n eigenmode basis, we have sensitivity with an expected $s/n > 1$ to ~340 temperature (co-polar) modes versus ~34 polarization (cross-polar) modes.

Detection of signal

Given that the data show remarkable consistency in χ^2 tests of the difference data vectors, the χ^2 values of the sum data vectors can be used to test for the presence of sky signal, independently of the likelihood analysis methods described below. In the co-polar data, all splits and subsets show highly significant χ^2 values (PTE $< 1 \times 10^{-16}$, the precision to which we calculate the cumulative distribution function).

For the cross-polar data, the sum data vector χ^2 values for the high s/n subsets show high significance, with the PTE $< 1 \times 10^{-6}$ for all $s/n > 1$ subsets in Table 1. This simple and powerful test indicates that we have detected, with high significance, the presence of a polarized signal in the data, and that this signal is repeatable in all of the data splits. The polarization map shown in Fig. 1 gives a visual representation of this repeatable polarization signal. Shown are the epoch split sum and difference polarization maps, con-

Table 1 χ^2 **Consistency tests for a selection of data splits and subsets**

Temperature data

		Difference			Sum	
Split type	Subset	d.f.	χ^2	PTE	χ^2	PTE
Year	Full	1,448	1,474.2	0.31	23,188.7	$<1 \times 10^{-16}$
	$s/n > 1$	320	337.1	0.24	21,932.2	$<1 \times 10^{-16}$
	l range 0–245	184	202.6	0.17	10,566.3	$<1 \times 10^{-16}$
	l range 0–245 high s/n	36	38.2	0.37	10,355.1	$<1 \times 10^{-16}$
	l range 245–420	398	389.7	0.61	7,676.0	$<1 \times 10^{-16}$
	l range 245–420 high s/n	79	88.9	0.21	7,294.4	$<1 \times 10^{-16}$
	l range 420–596	422	410.5	0.65	3,122.5	$<1 \times 10^{-16}$
	l range 420–596 high s/n	84	73.5	0.79	2,727.8	$<1 \times 10^{-16}$
	l range 596–772	336	367.8	0.11	1,379.5	$<1 \times 10^{-16}$
	l range 596–772 high s/n	67	82.3	0.10	991.8	$<1 \times 10^{-16}$
	l range 772–1100	108	103.7	0.60	444.4	$<1 \times 10^{-16}$
	l range 772–1100 high s/n	21	22.2	0.39	307.7	$<1 \times 10^{-16}$
Epoch	Full	1,520	1,546.3	0.31	32,767.2	$<1 \times 10^{-16}$
	$s/n > 1$	348	366.5	0.24	31,430.0	$<1 \times 10^{-16}$
Azimuth range	Full	1,520	1,542.6	0.34	32,763.8	$<1 \times 10^{-16}$
	$s/n > 1$	348	355.2	0.38	31,426.9	$<1 \times 10^{-16}$
Faceplate position	Full	1,318	1,415.2	0.03	27,446.5	$<1 \times 10^{-16}$
	$s/n > 1$	331	365.3	0.09	26,270.1	$<1 \times 10^{-16}$
Stokes state	Full	1,524	1,556.6	0.27	33,050.6	$<1 \times 10^{-16}$
	$s/n > 1$	350	358.2	0.37	31,722.5	$<1 \times 10^{-16}$

Polarization data

		Difference			Sum	
Split type	Subset	d.f.	χ^2	PTE	χ^2	PTE
Year	Full	2,896	2,949.4	0.24	2,925.2	0.35
	$s/n > 1$	30	34.4	0.27	82.4	8.7×10^{-7}
	l range 0–245	368	385.9	0.25	315.0	0.98
	l range 0–245 high s/n	73	61.0	0.84	64.5	0.75
	l range 245–420	796	862.2	0.05	829.4	0.20
	l range 245–420 high s/n	159	176.0	0.17	223.8	5.4×10^{-4}
	l range 420–596	844	861.0	0.33	837.3	0.56
	l range 420–596 high s/n	168	181.3	0.23	189.7	0.12
	l range 596–772	672	648.1	0.74	704.4	0.19
	l range 596–772 high s/n	134	139.5	0.35	160.0	0.06
	l range 772–1100	216	192.3	0.88	239.1	0.13
	l range 772–1100 high s/n	43	32.3	0.88	47.6	0.29
Epoch	Full	3,040	2,907.1	0.96	3,112.2	0.18
	$s/n > 1$	34	29.2	0.70	98.6	3.3×10^{-8}
Azimuth range	Full	3,040	3,071.1	0.34	3,112.9	0.17
	$s/n > 1$	34	38.7	0.27	98.7	3.3×10^{-8}
Faceplate position	Full	2,636	2,710.4	0.15	2,722.2	0.12
	$s/n > 1$	32	43.6	0.08	97.5	1.6×10^{-8}

Results of χ^2 consistency tests for a representative selection of splits and subsets of the combined 2001–02 data set. Visibility data containing the same sky signal is split to form two data vectors; using the instrument noise model, the χ^2 statistic is then calculated on both the difference and sum data vectors. Also tabulated are the number of degrees of freedom (d.f.), and probability to exceed (PTE) the value in the χ^2 cumulative distribution function, to show the significance of the result (PTE values indicated as $<1 \times 10^{-16}$ are zero to the precision with which we calculate the χ^2 cumulative distribution function). Difference data χ^2 values test for systematic effects in the data, while comparisons with sum data values test for the presence of a repeatable sky signal. Temperature (co-polar) data are visibility data in which the polarizers from both receivers are in the left (LL Stokes state) or right (RR Stokes state) circularly polarized state; polarization (cross-polar) data are those in which the polarizers are in opposite states (LR or RL Stokes state). The '$s/n > 1$' subset is the subset of s/n eigenmodes > 1 and the l range high s/n subsets are the 20% highest s/n modes within the given l range. See 'χ^2 tests' section for further description of the data split types and subsets. We have calculated 296 χ^2 values for various split types and subsets, with no obvious trends that would indicate systematic contamination of the data.

structed using the same 34 modes with $s/n > 1$ of the polarization data in the concordance model s/n eigenmode basis that appear in Table 1. The sum map shows a repeatable polarized signal, while the difference map is consistent with instrument noise.

It is possible to calculate a similar χ^2 statistic for the data vector formed from the complete, unsplit data set. Combining all the data without the requirement of forming two equally weighted subsets should yield minimal noise, albeit without an exactly corresponding null (that is, difference) test. Recalculating the s/n eigenmodes for this complete cross-polar data vector gives 36 modes with expected $s/n > 1$, for which $\chi^2 = 98.0$ with a PTE $= 1.2 \times 10^{-7}$. This significance is similar to those from the sum data vectors under the various splits, which actually divide the data fairly equally and so are nearly optimal. It should be noted that our focus so far has been to test the instrumental noise model, and we have not dealt with the small cross-polar signal expected as a result of the off-axis leakage. As noted in the 'Off-axis leakage' subsection, it is not possible to correct the data elements directly for this effect, but we can account for it in calculating these χ^2 results by including the expected covariance of this leakage signal (see 'Theory covariance matrix' subsection) in the noise matrix C_N. Again recalculating the s/n eigenmodes, we find 34 cross-polar modes with $s/n > 1$ which give a $\chi^2 = 97.0$ and a PTE $= 5.7 \times 10^{-8}$, a significance similar to before. The off-axis leakage is also included in the likelihood analyses, where it is again found to have an insignificant impact on the results.

The likelihood analysis described in the following sections makes use of all of the information in our data set. Such an analysis, in principle, may yield statistically significant evidence of a signal even in cases of data sets for which it is not possible to isolate any individual modes which have average $s/n > 1$. However, the existence of such modes in our data set, which has resulted from our strategy of integrating deeply on a limited patch of sky, allows us to determine the presence of the signal with the very simple analysis described above. It also reduces sensitivity to the noise model estimation in the likelihood results that we report next. Finally, it gives our data set greater power to exclude the possibility of no signal than it might have had if we had observed more modes but with less s/n in each.

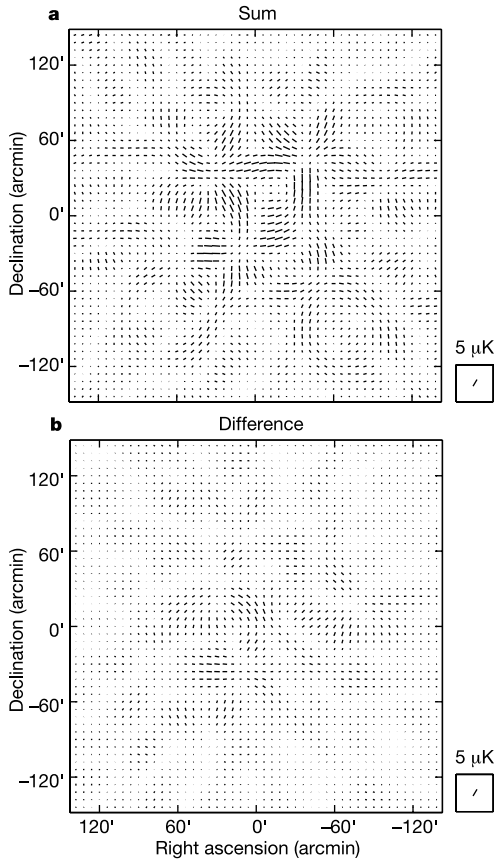

Figure 1 Polarization maps formed from high signal/noise eigenmodes. Shown are maps constructed from polarized data sets that have been split by epoch, and formed into sum (**a**) or difference (**b**) data vectors, as reported in section 'χ^2 tests'. In order to isolate the most significant signal in our data, we have used only the subset of 34 eigenmodes which, under the concordance model, are expected to have average signal/noise (s/n) > 1. Because the maps have only 34 independent modes, they exhibit a limited range of morphologies, and unlike conventional interferometer maps, these s/n selected eigenmodes reflect the taper of the primary beam, even when no signal is present. This is visually apparent in the difference map (**b**), which is statistically consistent with noise. Comparison of the difference map to the sum map (**a**) illustrates a result also given numerically for this split/subset in Table 1: that these individual modes in the polarized data set show a significant signal.

Likelihood analysis formalism

The preceding section gives strong evidence for the presence of a signal in our polarization data. We now examine that signal using the standard tool of likelihood analysis. In such an analysis, the covariance of the signal, $C_T(\kappa)$, is modelled in terms of parameters κ appropriate for describing the temperature and polarization anisotropy of the CMB. The covariance of the data vector is modelled $C(\kappa) \equiv C_T(\kappa) + C_N$, where C_N is the noise covariance matrix. Given our data vector $\mathbf{\Delta}$, the likelihood of the model specified by the parameter vector κ is the probability of our data vector given that model:

$$L(\kappa) = P(\mathbf{\Delta} \mid \kappa) \propto \det(C(\kappa))^{-1/2} \exp\left(-\frac{1}{2}\mathbf{\Delta}^t C(\kappa)^{-1}\mathbf{\Delta}\right) \quad (1)$$

Although the full likelihood function itself is the most basic result of the likelihood analysis, it is useful to identify and report the values of the parameters that maximize the likelihood (so-called maximum likelihood (ML) estimators). Uncertainties in the parameter values can be estimated by characterizing the shape of the likelihood surface, as discussed further in the 'Reporting of likelihood results' subsection.

The CMB power spectra

The temperature and polarization anisotropy of the CMB can be characterized statistically by six angular power spectra: three that give the amplitudes of temperature, E-mode and B-mode polarization anisotropy as a function of angular scale, and three that describe correlations between them. These spectra are written C_l^X, with $X = \{T, E, B, TE, TB, EB\}$. In our likelihood analyses, we choose various parameterizations of these spectra to constrain.

For a given cosmological model, these spectra can be readily calculated using efficient, publicly available Boltzmann codes[54]. Details of how to define these spectra in terms of all-sky multipole expansions of the temperature and linear polarization of the CMB radiation field are available in the literature (see refs 15 and 16). For DASI's 3.4° field of view, a flat sky approximation is appropriate[55], so that the spectra may be defined somewhat more simply[26]. In this approximation the temperature angular power spectrum is defined:

$$C_l^T \simeq C^T(u) \equiv \left\langle \frac{\tilde{T}^*(\mathbf{u})\tilde{T}(\mathbf{u})}{T_{CMB}^2} \right\rangle \quad (2)$$

where $\tilde{T}(\mathbf{u})$ is the Fourier transform of $T(\mathbf{x})$, T_{CMB} is the mean temperature of the CMB, and $l/2\pi = u$ gives the correspondence between multipole l and Fourier radius $u = |\mathbf{u}|$. The other spectra in

the flat sky approximation are similarly defined, for example, $C^{TE}(u) \equiv \langle \tilde{T}^{*}(\mathbf{u})\tilde{E}(\mathbf{u})/T^{2}_{\mathrm{CMB}} \rangle$. The relationship between $\tilde{E}$, $\tilde{B}$ and the linear polarization Stokes parameters Q and U is:

$$\tilde{Q}(\mathbf{u}) = \cos(2\chi)\tilde{E}(\mathbf{u}) - \sin(2\chi)\tilde{B}(\mathbf{u})$$

$$\tilde{U}(\mathbf{u}) = \sin(2\chi)\tilde{E}(\mathbf{u}) + \cos(2\chi)\tilde{B}(\mathbf{u}) \quad (3)$$

where $\chi = \arg(\mathbf{u})$ and the polarization orientation angle defining Q and U are both measured on the sky from north through east.

Theory covariance matrix

The theory covariance matrix is the expected covariance of the signal component of the data vector, $\mathbf{C}_T \equiv \langle \mathbf{s}\mathbf{s}^{t} \rangle$. The signals measured by the visibilities in our data vector for a given baseline $\mathbf{u}_i$ (after calibration and leakage correction) are:

$$V^{\mathrm{RR}}(\mathbf{u}_i) = \alpha_i \int \mathrm{d}\mathbf{x}\, A(\mathbf{x}, \nu_i)[T(\mathbf{x}) + V(\mathbf{x})]\, \mathrm{e}^{-2\pi i \mathbf{u}_i \cdot \mathbf{x}}$$

$$V^{\mathrm{LL}}(\mathbf{u}_i) = \alpha_i \int \mathrm{d}\mathbf{x}\, A(\mathbf{x}, \nu_i)[T(\mathbf{x}) - V(\mathbf{x})]\, \mathrm{e}^{-2\pi i \mathbf{u}_i \cdot \mathbf{x}}$$

$$V^{\mathrm{RL}}(\mathbf{u}_i) = \alpha_i \int \mathrm{d}\mathbf{x}\, A(\mathbf{x}, \nu_i)[Q(\mathbf{x}) + iU(\mathbf{x})]\, \mathrm{e}^{-2\pi i \mathbf{u}_i \cdot \mathbf{x}}$$

$$V^{\mathrm{LR}}(\mathbf{u}_i) = \alpha_i \int \mathrm{d}\mathbf{x}\, A(\mathbf{x}, \nu_i)[Q(\mathbf{x}) - iU(\mathbf{x})]\, \mathrm{e}^{-2\pi i \mathbf{u}_i \cdot \mathbf{x}} \quad (4)$$

where $A(\mathbf{x}, \nu_i)$ specifies the beam power pattern at frequency ν_i, $T(\mathbf{x})$, $Q(\mathbf{x})$, $U(\mathbf{x})$, and $V(\mathbf{x})$ are the four Stokes parameters in units of CMB temperature (μK), and $\alpha_i = \partial B_{\mathrm{Planck}}(\nu_i, T_{\mathrm{CMB}})/\partial T$ is the appropriate factor for converting from these units to flux density (Jy). The co-polar visibilities V^{RR} and V^{LL} are sensitive to the Fourier transform of the temperature signal $T(\mathbf{x})$ and circular polarization component $V(\mathbf{x})$ (expected to be zero). The cross-polar visibilities V^{RL} and V^{LR} are sensitive to the Fourier transform of the linear polarization components Q and U. Using equation (3), it can be seen that pairwise combinations of the visibilities are direct measures of nearly pure T, E and B Fourier modes on the sky, so that the data set easily lends itself to placing independent constraints on these power spectra.

We construct the theory covariance matrix as the sum of components for each parameter in the analysis:

$$C_{\mathrm{T}}(\kappa) = \sum_{p} \kappa_p B^{p}_{\mathrm{T}} \quad (5)$$

From equations (2)–(4), it is possible to derive a general expression for the matrix elements of a theory matrix component:

$$B^{p}_{\mathrm{T}ij} = \frac{1}{2}\alpha_i \alpha_j T^{2}_{\mathrm{CMB}} \int \mathrm{d}\mathbf{u}\; C^{X}(u)\tilde{A}(\mathbf{u}_i - \mathbf{u}, \nu_i) \times [\zeta_1 \tilde{A}(\mathbf{u}_j - \mathbf{u}, \nu_j) + \zeta_2 \tilde{A}(\mathbf{u}_j + \mathbf{u}, \nu_j)] \quad (6)$$

The coefficients ζ_1 and ζ_2 can take values $\{0, \pm 1, \pm 2\} \times \{\cos\{2\chi, 4\chi\}, \sin\{2\chi, 4\chi\}\}$ depending on the Stokes states (RR, LL, RL, LR) of each of the two baselines i and j and on which of the six spectra (T, E, B, TE, TB, EB) is specified by X. The integration may be limited to annular regions which correspond to l-ranges over which the power spectrum C^X is hypothesized to be relatively flat, or else some shape of the spectrum may be postulated.

Potentially contaminated modes in the data vector may be effectively projected out using a constraint matrix formalism[53]. This formalism can be used to remove the effect of point sources of known position without knowledge of their flux densities, as we described in ref. 6. This procedure can be generalized to include the case of polarized point sources. Although we have tested for the presence of point sources in the polarization power spectra using this method, in the final analysis we use constraint matrices to project point sources out of the temperature data only, and not the polarization data (see 'Point sources' subsection).

The off-axis leakage, discussed in the 'Off-axis leakage' subsection and in detail in ref. 51, has the effect of mixing some power from the temperature signal T into the cross-polar visibilities. Our model of the off-axis leakage allows us to write an expression for it analogous to equation (4), and to construct a corresponding theory covariance matrix component to account for it. In practice, this is a small effect, as discussed in the 'Systematic uncertainties' section.

Likelihood parameters

In the 'Likelihood results' section we present the results from nine separate likelihood analyses involving the polarization data, the temperature data, or both. Our choice of parameters with which to characterize the six CMB power spectra is a compromise between maximizing sensitivity to the signal and constraining the shape of the power spectra. In the different analyses we either characterize various power spectra with a single amplitude parameter covering all angular scales, or split the l-range into five bands over which spectra are approximated as piecewise-flat, in units of $l(l+1)C_l/(2\pi)$. Five bands were chosen as a compromise between too many for the data to bear and too few to capture the shape of the underlying power spectra. The l-ranges of these five bands are based on those of the nine-band analysis we used in ref. 6; we have simply combined the first four pairs of these bands, and kept the ninth as before. In some analyses we also constrain the frequency spectral indices of the temperature and polarization power spectra as a test for foreground contamination.

The l-range to which DASI has non-zero sensitivity is $28 < l < 1,047$. That range includes the first three peaks of the temperature power spectrum, and within it the amplitude of that spectrum, which we express in units $l(l+1)C_l/(2\pi)$, varies by a factor of about 4. Over this same range, the E-mode polarization spectrum is predicted to have four peaks while rising roughly as l^2 (in the same units), varying in amplitude by nearly two orders of magnitude[17]. The TE correlation is predicted to exhibit a complex spectrum that in fact crosses zero five times in this range.

For the single bandpower analyses which maximize our sensitivity to a potential signal, the shape of the model power spectrum assumed will have an effect on the sensitivity of the result. In particular, if the assumed shape is a poor fit to the true spectrum preferred by the data, the results will be both less powerful and difficult to interpret. For temperature spectrum measurements, the most common choice in recent years has been the so-called flat bandpower, $l(l+1)C_l \propto$ constant, which matches the gross large-angle 'scale-invariant' power-law shape of that spectrum. Because of extreme variations predicted in the E and TE spectra over DASI's l-range, we do not expect a single flat bandpower parameterization to offer a good description of the entire data set (although in the 'E/B analysis' subsection we describe results of applying such an analysis to limited l-range subsets of data). A more appropriate definition of 'flat bandpower' for polarization measurements sensitive to large ranges of $l < 1{,}000$ might be $C_l \propto$ constant (or $l(l+1)C_l \propto l^2$). Other shapes have been tried, notably the gaussian autocorrelation function (by the PIQUE group[56]) which reduces to $C_l \propto$ constant at large scales and perhaps offers a better fit to the gross shape of the predicted E spectrum.

In our single band analyses, we have chosen a shape for our single bandpower parameters based on the predicted spectra for a cosmological model currently favoured by observations. The specific model that we choose—which we will call the concordance model—is a ΛCDM model with flat spatial curvature, 5% baryonic matter, 35% dark matter, 60% dark energy, and a Hubble constant of $65\,\mathrm{km\,s^{-1}\,Mpc^{-1}}$, ($\Omega_{\mathrm{b}} = 0.05$, $\Omega_{\mathrm{cdm}} = 0.35$, $\Omega_{\Lambda} = 0.60$, $h = 0.65$) and the exact normalization $C_{10} = 700\,\mu\mathrm{K}^2$. This concordance model was defined in ref. 50 as a good fit to the previous DASI temperature power spectrum and other observations. The concordance model spectra for T, E, and TE are shown in Fig. 4. The five flat

bandpower likelihood results shown in Fig. 4, and discussed in the next section, suggest that the concordance shaped spectra do indeed characterize the data better than any power-law approximation. In the '*E*/*B* analysis' subsection, we explicitly test the likelihood of the concordance model parameterization against that of the two power laws mentioned above, and find that the concordance model shape is strongly preferred by the data.

It should be noted that the likelihood analysis is always model dependent, regardless of whether a flat or shaped model is chosen for parameterization. To evaluate the expectation value of the results for a hypothesized theoretical power spectrum, we must use window functions appropriate for the parameters of the particular analysis. The calculation of such parameter window functions has previously been described, both generally[57,58], and with specific reference to polarization spectra[59]. In general, the parameter window function has a non-trivial shape (even for a flat bandpower analysis) which is dependent on the shape of the true spectra as well as the intrinsic sensitivity of the instrument as a function of angular scale. Parameter window functions for the *E*/*B* and *E*5/*B*5 polarization analysis are shown in Fig. 2, and will also be made available on our website (http://astro.uchicago.edu/dasi).

Likelihood evaluation

Prior to likelihood analysis, the data vector and the covariance matrices can be compressed by combining visibility data from nearby points in the (u, v) plane, where the signal is highly correlated. This reduces the computational time required for the analyses without a significant loss of information about the signal. All analyses were run on standard desktop computers.

For each analysis, we use an iterated quadratic estimator technique to find the ML values of our parameters[53]. To further characterize the shape of the likelihood function, in ref. 6 we used an offset log-normal approximation. Here, for improved accuracy in calculating confidence intervals and likelihood ratios, we explicitly map out the likelihood function by evaluating equation (1) over a uniform parameter grid large enough to enclose all regions of substantial likelihood. A single likelihood evaluation typically takes several seconds, so this explicit grid evaluation is impractical for the analyses which include five or more parameters. For each analysis we also implement a Markov chain evaluation of the likelihood function[60]. We find this to be a useful and efficient tool for mapping the likelihoods of these high-dimensional parameter spaces in the region of substantial likelihood. We have compared the Markov technique to the grid evaluation for the lower-dimensional analyses and found the results to be in excellent agreement. In all cases, the peak of the full likelihood evaluated with either technique is confirmed to coincide with the ML values returned by the iterated quadratic estimator.

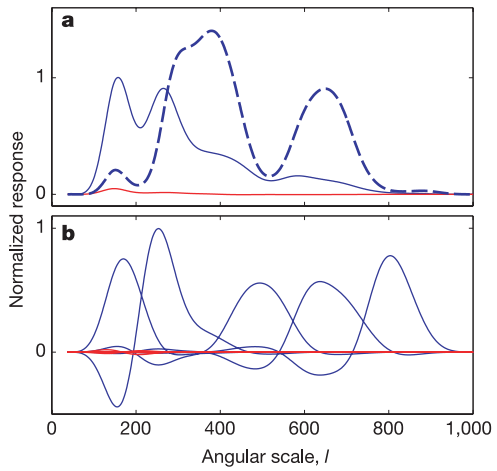

Figure 2 Parameter window functions, which indicate the angular scales over which the parameters in our analyses constrain the power spectra. **a**, The functions for the *E* parameter of our *E*/*B* analysis, with the solid blue curve indicating response to the *E* power spectrum and the solid red (much lower) curve indicating response of the same *E* parameter to the *B* spectrum. The blue dashed curve shows the result of multiplying the *E* window function by the concordance *E* spectrum, illustrating that for this CMB spectrum, most of the response of our experiment's *E* parameter comes from the region of the second peak ($300 \lesssim l \lesssim 450$), with a substantial contribution also from the third peak and a smaller contribution from the first. **b**, The *E*1 to *E*5 parameter window functions for the *E* power spectrum (blue) and *B* power spectrum (red, again much lower) from our *E*5/*B*5 analysis. All of these window functions are calculated with respect to the concordance model discussed in the text. DASI's response to *E* and *B* is very symmetric, so that *E* and *B* parameter window functions which are calculated with respect to a model for which $E = B$ are nearly identical, with the *E* and *B* spectral response reversed.

Simulations and parameter recovery tests

The likelihood analysis software was extensively tested through analysis of simulated data. The analysis software and data simulation software were independently authored, as a check for potential coding errors.

Simulated sky maps were generated from realizations of a variety of smooth CMB power spectra, including both the concordance spectrum and various non-concordance models, both with and without *E* and *B* polarization and *TE* correlations. Independent realizations of the sky were 'observed' to construct simulated visibilities with Fourier-plane sampling identical to the real data. The simulations were designed to replicate the actual data as realistically as possible and include artefacts of the instrumental polarization response and calibration, such as the on-axis and off-axis leakages and the cross-polar phase offset, described in the 'Measuring polarization with DASI' section, allowing us to test the calibration and treatment of these effects implemented in the analysis software.

Each of the analyses described in the 'Likelihood results' section was performed on hundreds of these simulated data sets with independent realizations of sky and instrument noise, both with noise variances that matched the real data, and with noise a factor of ten lower. In all cases, we found that the means of the ML estimators recovered the expectation values $\langle \kappa_p \rangle$ of each parameter without evidence of bias, and that the variance of the ML estimators was found to be consistent with the estimated uncertainty given by F^{-1} evaluated at $\langle \kappa \rangle$, where F is the Fisher matrix.

Reporting of likelihood results

Maximum likelihood (ML) parameter estimates reported in this paper are the global maxima of the multidimensional likelihood function. Confidence intervals for each parameter are determined by integrating (marginalizing) the likelihood function over the other parameters; the reported intervals are the equal-likelihood bounds which enclose 68% of this marginal likelihood distribution. This prescription corresponds to what is generally referred to as the highest posterior density (HPD) interval. When calculating these intervals we consider all parameter values, including non-physical ones, because our aim is simply to summarize the shape of the likelihood function. Values are quoted in the text using the convention 'ML (HPD-low to HPD-high)' to make clear that the confidence range is not directly related to the maximum likelihood value.

In the tabulated results, we also report marginalized uncertainties obtained by evaluating the Fisher matrix at the maximum likelihood model, that is, $(F^{-1})_{ii}^{1/2}$ for parameter i. Although in most cases, the two confidence intervals are quite similar, we regard the HPD interval as the primary result.

For parameters which are intrinsically positive we consider placing (physical) upper limits by marginalizing the likelihood

distribution as before, but excluding the unphysical negative values. We then test whether the 95% integral point has a likelihood smaller than that at zero; if it does we report an upper limit rather than a confidence interval.

We also report the parameter correlation matrices for our various likelihood analyses to allow the reader to gauge the degree to which each parameter has been determined independently. The covariance matrix is the inverse of the Fisher matrix and the correlation matrix, R, is defined as the covariance matrix normalized to unity on the diagonal, that is, $C = F^{-1}$ and $R_{ij} = C_{ij}/\sqrt{C_{ii}C_{jj}}$.

Goodness-of-fit tests

Using the likelihood function, we wish to determine if our results are consistent with a given model. For example, we would like to examine the significance of any detections by testing for the level of consistency with zero signal models, and we would like to determine if the polarization data are consistent with predictions of the standard cosmological model. We define as a goodness-of-fit statistic the logarithmic ratio of the maximum of the likelihood to its value for some model $\mathscr{H}_0$ described by parameters κ_0:

$$\Lambda(\mathscr{H}_0) \equiv -\log\left(\frac{L(\kappa_{\mathrm{ML}})}{L(\kappa_0)}\right)$$

The statistic Λ simply indicates how much the likelihood has fallen from its peak value down to its value at κ_0. Large values indicate inconsistency of the likelihood result with the model $\mathscr{H}_0$. To assess significance, we perform Monte Carlo (MC) simulations of this statistic under the hypothesis that $\mathscr{H}_0$ is true. From this, we can determine the probability, given $\mathscr{H}_0$ true, to obtain a value of Λ that exceeds the observed value, which we hereafter refer to as PTE.

When considering models which the data indicate to be very unlikely, sufficient sampling of the likelihood statistic becomes computationally prohibitive; our typical MC simulations are limited to only 1,000 realizations. In the limit that the parameter errors are normally distributed, our chosen statistic reduces to $\Lambda = \Delta\chi^2/2$. The integral over the χ^2 distribution is described by an incomplete gamma function;

$$\mathrm{PTE} = \frac{1}{\Gamma(N/2)}\int_{\Lambda}^{\infty} \mathrm{e}^{-x} x^{\frac{N}{2}-1}\,\mathrm{d}x$$

where $\Gamma(x)$ is the complete gamma function, and N is the number of parameters. Neither the likelihood function nor the distribution of the ML estimators is, in general, normally distributed, and therefore this approximation must be tested. In all cases where we can compute a meaningful PTE with MC simulations, we have done so and found the results to be in excellent agreement with the analytic approximation. Therefore, we are confident that adopting this approximation is justified. All results for PTE in this paper are calculated using this analytic expression unless otherwise stated.

Likelihood results

We have performed nine separate likelihood analyses to constrain various aspects of the signal in our polarization data, in our temperature data, or in both analysed together. The choice of parameters for these analyses and the conventions used for reporting likelihood results have been discussed in 'Likelihood parameters' and 'Reporting of likelihood results' subsections. Numerical results for the analyses described in this section are given in Tables 2, 3 and 4.

Polarization data analyses and *E* and *B* results

***E*/*B* analysis.** The E/B analysis uses two single-bandpower parameters to characterize the amplitudes of the E and B polarization spectra. As discussed in the 'Likelihood parameters' subsection, this analysis requires a choice of shape for the spectra to be parameterized. DASI has instrumental sensitivity to E and B that is symmetrical and nearly independent. Although the B spectrum is not expected to have the same shape as the E spectrum, we choose the same shape for both spectra in order to make the analysis also symmetrical.

We first compute the likelihood using a $l(l+1)C_l/2\pi = \text{constant}$ bandpower (commonly referred to as 'flat' bandpower) including data only from a limited l range in which DASI has high sensitivity; see Fig. 2. Using the range $300 < l < 450$ which includes 24% of the complete data set, we find the ML at flat bandpower values $E = 26.5\,\mu\mathrm{K}^2$ and $B = 0.8\,\mu\mathrm{K}^2$. The likelihood falls dramatically for the zero polarization 'nopol' model $E = 0, B = 0$. Marginalizing over B, we find $\Lambda(E = 0) = 16.9$ which, assuming the uncertainties are normally distributed, corresponds to a PTE of 5.9×10^{-9} or a significance of E detection of 5.8σ. As expected, changing the l range affects the maximum likelihood values and the confidence of detection; for example, shifting the centre of the above l range by ± 25 reduces the confidence of detection to 5.6σ and 4.8σ, respectively. Clearly it is desirable to perform the analysis over the entire l range sampled by DASI using a well motivated bandpower shape for the parameterization.

We considered three a priori shapes to check which is most appropriate for our data: the concordance E spectrum shape (as defined in 'Likelihood parameters'), and two power law alternatives, $l(l+1)C_l \propto \text{constant}$ (flat) and $l(l+1)C_l \propto l^2$. For each of these three cases, the point at $E = 0, B = 0$ corresponds to the same zero-polarization 'nopol' model, so that the likelihood ratios $\Lambda(\text{nopol})$ may be compared directly to assess the relative likelihoods of the best-fit models. For the $l(l+1)C_l \propto \text{constant}$ case, the ML flat bandpower values are $E = 6.8\,\mu\mathrm{K}^2$, $B = -0.4\,\mu\mathrm{K}^2$, with $\Lambda(\text{nopol}) = 4.34$. For the $l(l+1)C_l \propto l^2$ case, the ML values are $E = 5.1\,\mu\mathrm{K}^2$, $B = 1.2\,\mu\mathrm{K}^2$ (for $l(l+1)C_l/2\pi$ at $l = 300$), with $\Lambda(\text{nopol}) = 8.48$. For the concordance shape, the ML values are $E = 0.80$, $B = 0.21$ in units of the concordance E spectrum amplitude, with $\Lambda(\text{nopol}) = 13.76$. The likelihood of the best-fit model in the concordance case is a factor of 200 and 12,000 higher than those of the $l(l+1)C_l \propto l^2$ and $l(l+1)C_l \propto \text{constant}$ cases, respectively, and so compared to the concordance shape either of these is a very poor model for the data. The data clearly prefer the concordance shape, which we therefore use for the E/B and other single bandpower analyses presented in our results tables.

Figure 3 illustrates the result of the E/B concordance shape polarization analysis. The maximum likelihood value of E is 0.80 (0.56 to 1.10 at 68% confidence). For B, the result should clearly be regarded as an upper limit; 95% of the $B > 0$ likelihood (marginalized over E) lies below 0.59.

Figure 2a shows the parameter window functions relevant for this analysis. Note that the E parameter has very little sensitivity to B and vice versa—the purity with which DASI can separate these is remarkable. This is also demonstrated by the low correlation (-0.046) between the E and B parameters (see Table 2).

Assuming that the uncertainties in E and B are normally distributed ('Goodness-of-fit tests' section), the likelihood ratio $\Lambda(\text{nopol}) = 13.76$ implies a probability that our data are consistent with the zero-polarization hypothesis of $\mathrm{PTE} = 1.05 \times 10^{-6}$. Our data are highly incompatible with the no-polarization hypothesis. Marginalizing over B, we find $\Lambda(E = 0) = 12.1$ corresponding to detection of E-mode polarization at a PTE of 8.46×10^{-7} (or a significance of 4.92σ).

The likelihood ratio for the concordance model gives $\Lambda(E = 1, B = 0) = 1.23$, for which the Monte Carlo and analytic PTE are both 0.28. We conclude that our data are consistent with the concordance model.

However, given the precision to which the temperature power spectrum of the CMB is currently known, even within the ~7-parameter class of cosmological models often considered, the shape and amplitude of the predicted E-mode spectrum are still somewhat uncertain. To quantify this, we have taken the model grid generated for ref. 50 and calculated the expectation value of the

Table 2 **Results of likelihood analyses from polarization data**

Analysis	Parameter	l_{low}–l_{high}	ML est.	68% interval $(F^{-1})_{ii}^{1/2}$ error	Lower	Upper	UL (95%)	Units
E/*B*	*E*	–	0.80	±0.28	0.56	1.10	–	Fraction of concordance *E*
	B	–	0.21	±0.18	0.05	0.40	0.59	Fraction of concordance *E*
*E*5/*B*5	*E*1	28–245	−0.50	±0.8	−1.20	1.45	2.38	μK^2
	*E*2	246–420	17.1	±6.3	11.3	31.2	–	μK^2
	*E*3	421–596	−2.7	±5.2	−10.0	4.3	24.9	μK^2
	*E*4	597–772	17.5	±16.0	3.8	40.3	47.2	μK^2
	*E*5	773–1,050	11.4	±49.0	−32.5	92.3	213.2	μK^2
	*B*1	28–245	−0.65	±0.65	−1.35	0.52	1.63	μK^2
	*B*2	246–420	1.3	±2.4	−0.7	5.0	10.0	μK^2
	*B*3	421–596	4.8	±6.5	−0.6	13.5	17.2	μK^2
	*B*4	597–772	13.0	±14.9	1.6	31.0	49.1	μK^2
	*B*5	773–1,050	−54.0	±28.9	−77.7	−4.4	147.4	μK^2
E/β_E	*E*	–	0.84	±0.28	0.55	1.08	–	Fraction of concordance *E*
	β_E	–	0.17	±1.96	−1.63	1.92	–	Temperature spectral index
Scalar/Tensor	*S*	–	0.87	±0.29	0.62	1.18	–	Fraction of concordance *S*
	T	–	−14.3	±7.5	−20.4	−3.9	25.4	*T*/(*S* = 1)

The four corresponding parameter correlation matrices

*E*1	*E*2	*E*3	*E*4	*E*5	*B*1	*B*2	*B*3	*B*4	*B*5
1	−0.137	0.016	−0.002	0.000	−0.255	0.047	−0.004	0.000	0.000
	1	−0.117	0.014	−0.002	0.024	−0.078	0.004	0.000	0.000
		1	−0.122	0.015	−0.003	0.010	−0.027	0.003	−0.001
			1	−0.119	0.000	−0.001	0.002	−0.016	0.003
				1	0.000	0.000	0.000	0.002	−0.014
					1	−0.226	0.022	−0.002	0.000
						1	−0.097	0.011	−0.002
							1	−0.111	0.018
								1	−0.164
									1

E	*B*
1	−0.046
	1

E	β_E
1	−0.046
	1

S	*T*
1	−0.339
	1

ML est., maximum likelihood estimate. $(F^{-1})_{ii}^{1/2}$, Fisher matrix uncertainty for parameter *i* is evaluated at ML. UL, upper limit.

shaped band *E* parameter for each model using the window function shown in Fig. 2. We then take the distribution of these predicted *E* amplitudes, weighted by the likelihood of the corresponding model given our previous temperature results (using a common calibration uncertainty for the DASI temperature and polarization measurements). This yields a 68% credible interval for the predicted value of the *E* parameter of 0.90 to 1.11. As illustrated in Fig. 3a, our data are compatible with the expectation for *E* on the basis of existing knowledge of the temperature spectrum.

***E*5/*B*5.** Figure 4a and b show the results of a ten-parameter analysis characterizing the *E* and *B*-mode spectra using five flat bandpowers for each. Figure 2b shows the corresponding parameter window functions. Note the extremely small uncertainty in the measurements of the first bands *E*1 and *B*1.

To test whether these results are consistent with the concordance model, we calculate the expectation value for the nominal concordance model in each of the five bands, yielding $E = (0.8,14,13,37,16)$ and $B = (0,0,0,0,0)\,\mu K^2$. The likelihood ratio comparing this point in the ten-dimensional parameter space to the maximum gives $\Lambda = 5.1$, which for ten degrees of

Table 3 **Results of likelihood analyses from temperature data**

Analysis	Parameter	l_{low}–l_{high}	ML est.	68% interval $(F^{-1})_{ii}^{1/2}$ error	Lower	Upper	Units
T/β_T	*T*	–	1.19	±0.11	1.09	1.30	Fraction of concordance *T*
	β_T	–	−0.01	±0.12	−0.16	0.14	Temperature spectral index
*T*5	*T*1	28–245	6,510	±1,610	5,440	9,630	μK^2
	*T*2	246–420	1,780	±420	1,480	2,490	μK^2
	*T*3	421–596	2,950	±540	2,500	3,730	μK^2
	*T*4	597–772	1,910	±450	1,530	2,590	μK^2
	*T*5	773–1,050	3,810	±1,210	3,020	6,070	μK^2

The two corresponding parameter correlation matrices

*T*1	*T*2	*T*3	*T*4	*T*5
1	−0.101	0.004	−0.004	−0.001
	1	−0.092	−0.013	−0.011
		1	−0.115	−0.010
			1	−0.147
				1

T	β_T
1	0.023
	1

freedom results in a PTE of 0.42, indicating that our data are consistent with the expected polarization parameterized in this way. The *E*5/*B*5 results are highly inconsistent with the zero-polarization 'nopol' hypothesis, for which $\Lambda = 15.2$ with a PTE = 0.00073. This statistic is considerably weaker than the equivalent one obtained for the single band analysis in the 'E/B analysis' section, as expected from the higher number of degrees of freedom in this analysis. In this ten-dimensional space, all possible random deviations from the 'nopol' expectation values $E = (0,0,0,0,0)$, $B = (0,0,0,0,0)$ are treated equally in constructing the PTE for our Λ statistic. Imagining the 'nopol' hypothesis to be true, it would be far less likely to obtain a result in this large parameter space that is both inconsistent with 'nopol' at this level and at the same time is consistent with the concordance model, than it would be to obtain a result that is merely inconsistent with 'nopol' in some way at this level. It is the latter probability that is measured by the PTE for our Λ(nopol), explaining why this approach to goodness-of-fit weakens upon considering increasing numbers of parameters.

***E*/β_E.** We have performed a two-parameter analysis to determine the amplitude of the *E*-mode polarization signal as above and the frequency spectral index β_E of this signal relative to CMB (Fig. 5). As expected, the results for the *E*-mode amplitude are very similar to those for the *E*/*B* analysis described in the previous section. The spectral index constraint is not strong; the maximum likelihood value is $\beta_E = 0.17$ (-1.63 to 1.92). The result is nevertheless interesting in the context of ruling out possible foregrounds (see the 'Diffuse foregrounds' subsection below).

Scalar/tensor. Predictions exist for the shape of the *E* and *B*-mode spectra which would result from primordial gravity waves, also known as tensor perturbations, although their amplitude is not well constrained by theory. In a concordance-type model such tensor polarization spectra are expected to peak at $l \approx 100$. Assuming reasonable priors, current measurements of the temperature spectrum (in which tensor and scalar contributions will be mixed) suggest $T/S < 0.2$ (ref. 61), where this amplitude ratio is defined in terms of the tensor and scalar contributions to the temperature quadrupole C_2^T. We use the distinct polarization angular power spectra for the scalars (our usual concordance *E* shape, with $B = 0$) and the tensors (E_T and B_T) as two components of a likelihood analysis to constrain the amplitude parameters of these components. In principle, because the scalar *B*-mode spectrum is zero, this approach avoids the fundamental sample variance limitations arising from using the temperature spectrum alone. However, the *E*5/*B*5 analysis (see subsection '*E*5/*B*5') indicates that we have only upper limits to the *E*- and *B*-mode polarization at the angular scales most relevant ($l \lesssim 200$) for the tensor spectra. It is therefore not surprising that our limits on *T*/*S* derived from the polarization spectra as reported in Table 2 are quite weak.

Temperature data analyses and results for *T* spectrum

***T*/β_T.** Results are shown in Fig. 5 for a two-parameter analysis to determine the amplitude and frequency spectral index of the temperature signal. The bandpower shape used is that of the concordance *T* spectrum, and the amplitude parameter is expressed in units relative to that spectrum. The spectral index is relative to the CMB, so that 0 corresponds to a 2.73-K Planck spectrum. The amplitude of *T* has a maximum likelihood value of 1.19 (1.09 to 1.30), and the spectral index $\beta_T = -0.01$ (-0.16 to 0.14). Although the uncertainty in the temperature amplitude is dominated by sample variance, the spectral index is limited only by the sensitivity and fractional bandwidth of DASI. Owing to the extremely high *s*/*n* of the temperature data, the constraints on the spectral index are superior to those from previous DASI observations (ref. 6).

***T*5.** Fig. 4c shows the results of an analysis using five flat bands to characterize the temperature spectrum. These results are completely dominated by the sample variance in the differenced field. They are consistent with, although less precise than our previous temperature power spectra described in ref. 6; we include them here primarily to emphasize that DASI makes measurements simultaneously in all four Stokes parameters and is therefore able to

Table 4 **Results of likelihood analyses from joint temperature-polarization data set**

Analysis	Parameter	l_{low}–l_{high}	ML est.	68% interval			Units
				$(F^{-1})_{ii}^{1/2}$ error	Lower	Upper	
T/*E*/*TE*	*T*	–	1.13	±0.10	1.05	1.29	Fraction of concordance *T*
	E	–	0.77	±0.27	0.57	1.10	Fraction of concordance *E*
	TE	–	0.91	±0.38	0.45	1.37	Fraction of concordance *TE*
T/*E*/*TE*5	*T*	–	1.12	±0.10	1.09	1.31	Fraction of concordance *T*
	E	–	0.81	±0.28	0.71	1.36	Fraction of concordance *E*
	*TE*1	28–245	−24.8	±32.2	−55.3	24.7	μK^2
	*TE*2	246–420	92.3	±38.4	44.9	151.1	μK^2
	*TE*3	421–596	−10.5	±48.2	−60.1	52.0	μK^2
	*TE*4	597–772	−66.7	±74.3	−164.6	9.5	μK^2
	*TE*5	773–1050	20.0	±167.9	−130.3	172.3	μK^2
T/*E*/*B*/*TE*/*TB*/*EB*	*T*	–	1.13	±0.10	1.03	1.27	Fraction of concordance *T*
	E	–	0.75	±0.26	0.59	1.19	Fraction of concordance *E*
	B	–	0.20	±0.18	0.11	0.52	Fraction of concordance *E*
	TE	–	1.02	±0.37	0.53	1.49	Fraction of concordance *TE*
	TB	–	0.53	±0.32	0.08	0.82	Fraction of concordance *TE*
	EB	–	−0.16	±0.16	−0.38	0.01	Fraction of concordance *E*

The three parameter correlation matrices

T	*E*	*TE*1	*TE*2	*TE*3	*TE*4	*TE*5
1	0.026	−0.071	0.202	−0.018	−0.075	0.0(
	1	−0.067	0.339	−0.023	−0.090	0.008
		1	−0.076	0.006	0.011	−0.001
			1	−0.078	−0.039	0.004
				1	−0.056	0.004
					1	−0.066
						1

T	*E*	*B*	*TE*	*TB*	*EB*
1	0.026	0.004	0.230	0.136	0.033
	1	−0.027	0.320	−0.040	−0.182
		1	−0.027	0.219	−0.190
			1	−0.150	0.109
				1	0.213
					1

T	*E*	*TE*
1	0.017	0.207
	1	0.282
		1

measure temperature as well as polarization anisotropy. Note that these results and those for T/β_T have not been corrected for residual point sources.

Joint analyses and cross spectra results

T/E/TE. Figure 6 shows the results of a three-parameter single bandpower analysis of the amplitudes of the *T* and *E* spectra, and the *TE* cross-correlation spectrum. As before, bandpower shapes based on the concordance model are used. The *T* and *E* constraints are, as expected, very similar to those from the E/B, E/β_E and T/β_T analyses described above. The new result here is *TE* which has a maximum likelihood value of 0.91 (0.45 to 1.37). Note that in contrast to the two-dimensional likelihoods shown in other figures, here the contours show apparent evidence of correlation between the two parameters; the parameter correlation coefficients from Table 4 are 0.28 for *E*/*TE* and 0.21 for *T*/*TE*.

Marginalizing over *T* and *E*, we find that the likelihood of *TE* peaks very near 1, so that $\Lambda(TE = 1) = 0.02$ with a PTE of 0.857. For the 'no cross-correlation' hypothesis, $\Lambda(TE = 0) = 1.85$ with an analytic PTE of 0.054 (the PTE calculated from Monte Carlo simulations is 0.047). This result represents a detection of the expected *TE* correlation at 95% confidence and is particularly interesting in that it suggests a common origin for the observed temperature and polarization anisotropy.

It has been suggested that an estimator of *TE* cross-correlation constructed using a $TE = 0$ prior may offer greater immunity to systematic errors[59]. We have confirmed that applying such a technique to our data yields similar results to the above likelihood analysis, with errors slightly increased as expected.

T/E/TE5. We have performed a seven-parameter analysis using single shaped band powers for *T* and *E*, and five flat bandpowers for the *TE* cross-correlation; the *TE* results from this are shown in Fig. 4d. In this analysis the *B*-mode polarization has been explicitly set to zero. Again, the *T* and *E* constraints are similar to the values for the other analyses where these parameters appear. The *TE* bandpowers are consistent with the predictions of the concordance model.

T/E/B/TE/TB/EB. Finally, we describe the results of a six shaped bandpower analysis for the three individual spectra *T*, *E* and *B*, together with the three possible cross-correlation spectra *TE*, *TB* and *EB*. We include the *B* cross-spectra for completeness, though there is little evidence for any *B*-mode signal. Because there are no predictions for the shapes of the *TB* or *EB* spectra (they are expected to be zero), we preserve the symmetry of the analysis between *E* and *B* by simply parameterizing them in terms of the *TE* and *E* spectral shapes. The results for *T*, *E*, *B* and *TE* are similar to those obtained before, with no detection of *EB* or *TB*.

Systematic uncertainties

Noise, calibration, offsets and pointing

To assess the effect of systematic uncertainties on the likelihood results, we have repeated each of the nine analyses with alternative assumptions about the various effects that we have identified which reflect the range of uncertainty on each.

Much of the effort of the data analysis presented in this paper has gone into investigating the consistency of the data with the noise model as discussed in the 'Noise model' subsection. We find no discrepancies between complementary noise estimates on different timescales, to a level $\ll 1\%$. As discussed in the 'χ^2 tests' subsection, numerous consistency tests on subsets of the co-polar and

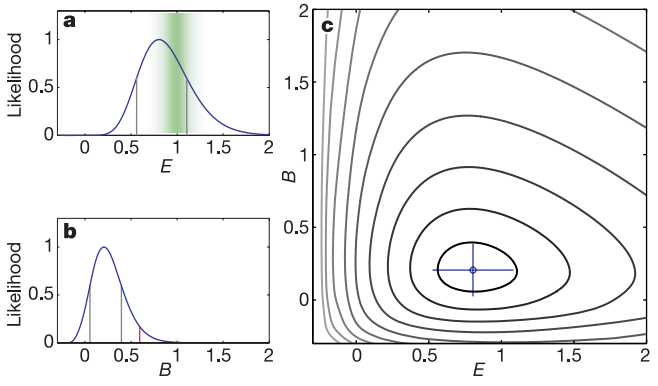

Figure 3 Results from the two-parameter shaped bandpower *E*/*B* polarization analysis. An *E*-mode power spectrum shape as predicted for the concordance model is assumed, and the units of amplitude are relative to that model. The same shape is assumed for the *B*-mode spectrum. **c**, The point shows the maximum likelihood value with the cross indicating Fisher matrix errors. Likelihood contours are placed at levels $\exp(-n^2/2)$, $n = 1,2\ldots$, relative to the maximum, that is, for a normal distribution, the extrema of these contours along either dimension would give the marginalized *n*-sigma interval. **a**, **b**, The corresponding single parameter likelihood distributions marginalized over the other parameter. Note the steep fall in likelihood toward low power values; this likelihood shape (similar to a χ^2 distribution) is typical for positive-definite parameters for which a limited number of high *s*/*n* modes are relevant. The grey lines enclose 68% of the total likelihood. The red line indicates the 95% confidence upper limit on *B*-mode power. The green band shows the distribution of *E* expectation values for a large grid of cosmological models weighted by the likelihood of those models given our previous temperature result (see ref. 50).

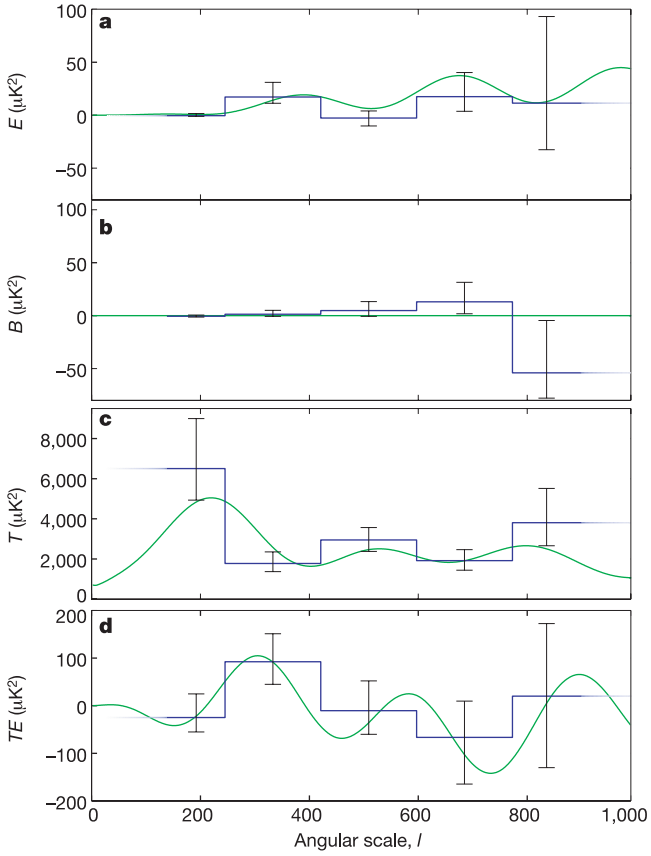

Figure 4 Results from several likelihood analyses. The ten-parameter *E*5/*B*5 polarization analysis is shown in **a** and **b**. The *T*5 temperature analysis is shown in **c** and the five *TE* bands from the *T*/*E*/*TE*5 joint analysis are shown in **d**. All the results are shown in flat bandpower units of $l(l+1)C_l/(2\pi)$. The blue line shows the piecewise flat bandpower model for the maximum likelihood parameter values, with the error bars indicating the 68% central region of the likelihood of each parameter, marginalizing over the other parameter values (analogous to the grey lines in Fig. 3a and b). In each case the green line is the concordance model.

cross-polar visibility data show no evidence for an error in the noise scaling to a similar level. When we re-evaluate each of the analyses described in the 'Likelihood results' section with the noise scaled by 1%, the shift in the maximum likelihood values for all parameters is entirely negligible.

In the 'Noise model' subsection, we reported evidence of some detectable noise correlations between real/imaginary visibilities and between visibilities from different bands of the same baseline. When either or both of these noise correlations are added to the covariance matrix at the measured level, the effects are again negligible: the most significant shift is in the highest-l band of the E spectrum from the $E5/B5$ analysis (see the '$E5/B5$' subsection), where the power shifts by about $2\,\mu K^2$.

Errors in the determination of the absolute cross-polar phase offsets will mix power between E and B; these phase offsets have been independently determined from wire-grid calibrations and observations of the Moon, and found to agree to within the measurement uncertainties of about 0.4° (ref. 51). Reanalysis of the data with the measured phase offsets shifted by 2° demonstrates that the likelihood results are immune to errors of this magnitude: the most significant effect occurs in the highest-l band of the TE spectrum from the $T, E, TE5$ analysis (see the '$T/E/TE5$' subsection), where the power shifts by about $30\,\mu K^2$.

The on-axis leakages described in the 'On-axis leakage' subsection will mix power from T into E and B, and the data are corrected for this effect in the course of reduction, before input to any analyses. When the likelihood analyses are performed without the leakage correction, the largest effects appear in the shaped TE amplitude analysis (see '$T/E/TE$' subsection), and the lowest-l band of $TE5$ from the $T, E, TE5$ analysis (see the '$T/E/TE5$' subsection); all shifts are tiny compared to the 68% confidence intervals. As the leakage correction itself has little impact on the results, the uncertainties in the correction, which are at the $< 1\%$ level, will have no noticeable effect.

As described in the 'Off-axis leakage' subsection, the off-axis leakage from the feeds is a more significant effect, and is accounted for in the likelihood analysis by modelling its contribution to the covariance matrix. When this correction is not applied, the E, B results (see 'E/B analysis' subsection) shift by about 4% and 2%, respectively, as expected from simulations of this effect. Although this bias is already small, the simulations show that the correction removes it completely to the degree to which we understand the off-axis leakage. Uncertainties in the leakage profiles of the order of the fit residuals (see ref. 51) lead to shifts of less than 1%.

The pointing accuracy of the telescope is measured to be better than 2 arcmin and the root-mean-square tracking errors are < 20 arcsec; as we discussed in refs 49 and 6, this is more than sufficient for the characterization of CMB anisotropy at the much larger angular scales measured by DASI.

Absolute calibration of the telescope was achieved through measurements of external thermal loads, transferred to the calibrator RCW38. The dominant uncertainty in the calibration is due to temperature and coupling of the thermal loads. As reported in ref. 6, we estimate an overall calibration uncertainty of 8% (1σ), expressed as a fractional uncertainty on the C_l bandpowers (4% in $\Delta T/T$). This applies equally to the temperature and polarization data presented here.

Foregrounds

Point sources. The highest-sensitivity point-source catalogue in our observing region is the 5-GHz PMN survey[62]. For our first-season temperature analysis described in refs 49 and 6 we projected out known sources using this catalogue. We have kept this procedure for the temperature data presented here, projecting the same set of sources as before.

Unfortunately the PMN survey is not polarization sensitive. We note that the distribution of point-source polarization fractions is approximately exponential (see below). Total intensity is thus a poor indicator of polarized intensity and it is therefore not sensible to project out the PMN sources in our polarization analysis.

Our polarization fields were selected for the absence of any significant point-source detections in the first-season data. No significant detections are found in the 2001–02 data, either in the

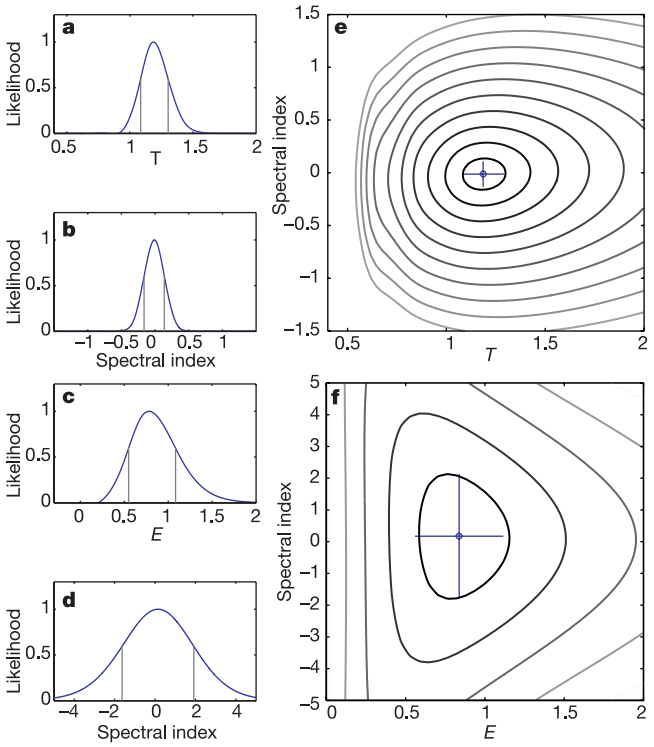

Figure 5 Results of shaped bandpower amplitude/spectral-index analyses. **a**, **b**, **e**, The T/β_T temperature analysis assuming the T power spectrum shape as predicted for the concordance model, and in units relative to that model. The layout of the plot is analogous to Fig. 3. Spectral index is relative to the CMB blackbody—in these units, synchrotron emission would be expected to have an index of approximately −3. **c**, **d**, **f**, Results of the similar E/β_E analysis performed on the polarization data.

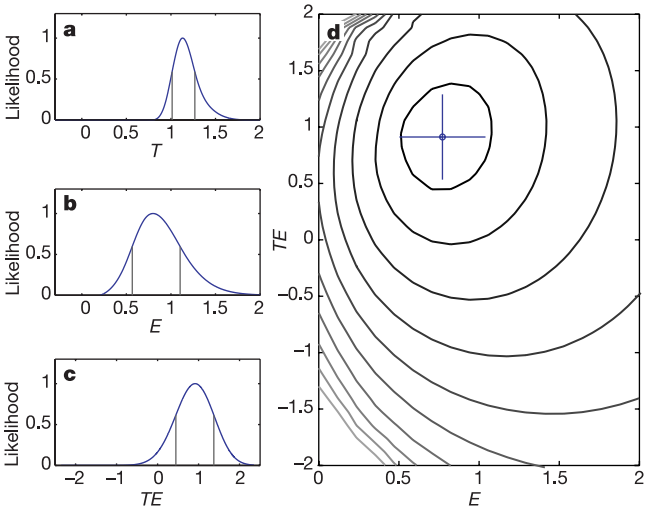

Figure 6 Results from the three-parameter shaped bandpower $T/E/TE$ joint analysis. Spectral shapes as predicted for the concordance model are assumed (**a**–**c**) and the units are relative to that model. The layout of the plot is analogous to Fig. 3. The two-dimensional distribution in **d** is marginalized over the T dimension.

temperature data, which are dominated by CMB anisotropy, or in the polarization data.

To calculate the expected contribution of undetected point sources to our polarization results we would like to know the distribution of polarized flux densities, but unfortunately no such information exists in our frequency range. However, to make an estimate, we use the distribution of total intensities, and then assume a distribution of polarization fractions. We know the former distribution quite well from our own first-season 32-field data where we detect 31 point sources and determine that $dN/dS_{31} = (32 \pm 7)S^{(-2.15\pm0.20)}\,\mathrm{Jy}^{-1}\,\mathrm{sr}^{-1}$ in the range 0.1 to 10 Jy. This is consistent, when extrapolated to lower flux densities, with a result from the CBI experiment valid in the range 5–50 mJy (ref. 63). The distribution of point source polarization fractions at 5 GHz can be characterized by an exponential with a mean of 3.8% (ref. 64); data of somewhat lower quality at 15 GHz are consistent with the same distribution[65]. Qualitatively, we expect the polarization fraction of synchrotron-dominated sources initially to rise with frequency, and then reach a plateau or fall, with the break point at frequencies $\ll$5 GHz (see ref. 66 for an example). In the absence of better data we have conservatively assumed that the exponential distribution mentioned above continues to hold at 30 GHz.

We proceed to estimate the effect of point sources by Monte Carlo simulation, generating realizations using the total intensity and polarization fraction distributions mentioned above. For each realization, we generate simulated DASI data by adding a realization of CMB anisotropy and appropriate instrument noise. The simulated data are tested for evidence of point sources and those realizations that show statistics similar to the real data are kept. The effect of off-axis leakage, which we describe and quantify in ref. 51, is included in these calculations.

When the simulated data are passed through the *E*/*B* analysis described in the '*E*/*B* analysis' subsection, the mean bias of the *E* parameter is 0.04 with a standard deviation of 0.05; in 95% of cases the shift distance in the *E*/*B* plane is less than 0.13. We conclude that the presence of point sources consistent with our observed data has a relatively small effect on our polarization results.

Diffuse foregrounds. In ref. 51, we find no evidence for contamination of the temperature data by synchrotron, dust or free–free emission, as confirmed by the limits on the temperature spectral index presented in the 'T/β_T' subsection. The expected fractional polarization of the CMB is of order 10%, while the corresponding number for free–free emission is less than 1%. Diffuse thermal dust emission may be polarized by several per cent (see for example ref. 67), although we note that polarization of the admixture of dust and free–free emission observed with DASI in NGC 6334 is $\ll$1% (see ref. 51). Likewise, emission from spinning dust is not expected to be polarized at detectable levels[68]. Therefore if free–free and dust emission did not contribute significantly to our temperature anisotropy results they are not expected to contribute to the polarization. Synchrotron emission on the other hand can in principle be up to 70% polarized, and is by far the greatest concern; what was a negligible contribution in the temperature case could be a significant one in polarization.

There are no published polarization maps in the region of our fields. Previous attempts to estimate the angular power spectrum of polarized synchrotron emission have been guided by surveys of the Galactic plane at frequencies of 1–3 GHz (refs 69 and 70). These maps show much more small-scale structure in polarization than in temperature, but this is mostly induced by Faraday rotation[71], an effect which is negligible at 30 GHz. In addition, because synchrotron emission is highly concentrated in the disk of the Galaxy it is not valid to assume that the angular power spectrum at low Galactic latitudes has much to tell us about that at high latitudes[72].

Our fields lie at Galactic latitude $-58.4°$ and $-61.9°$. The brightness of the IRAS 100 μm and Haslam 408 MHz (ref. 52) maps within our fields lie at the 6% and 25% points, respectively, of the integral distributions taken over the whole sky. There are several strong pieces of evidence from the DASI data set itself that the polarization results described in this paper are free of significant synchrotron contamination. The significant *TE* correlation shown in Fig. 6 indicates that the temperature and *E*-mode signal have a common origin. The tight constraints on the temperature anisotropy spectral index require that this common origin has a spectrum consistent with CMB. Galactic synchrotron emission is known to have a temperature spectral index of -2.8 (ref. 73), with evidence for steepening to -3.0 at frequencies above 1–2 GHz (ref. 74). At frequencies where Faraday depolarization is negligible (>10 GHz), the same index will also apply for polarization. The dramatically tight constraint on the temperature spectral index of $\beta_T = 0.01$ (-0.16 to 0.14) indicates that any component of the temperature signal coming from synchrotron emission is negligibly small in comparison to the CMB. More directly, the constraint on the *E*-mode spectral index $\beta_E = 0.17$ (-1.63 to 1.92) disfavours synchrotron polarization at nearly 2σ. A third, albeit weaker, line of argument is that a complex synchrotron emitting structure is not expected to produce a projected brightness distribution which prefers *E*-mode polarization over *B*-mode[75]. Therefore, the result in Fig. 3 could be taken as further evidence that the signal we are seeing is not due to synchrotron emission.

Discussion

This paper presents several measures of the confidence with which CMB polarization has been detected with DASI. Which measure is preferred depends on the desired level of statistical rigour and independence from a priori models of the polarization. The χ^2 analyses in the 'χ^2 tests' subsection offer the most model-independent results, although the linear combinations of the data used to form the *s*/*n* eigenmodes are selected by consideration of theory and the noise model. For the high *s*/*n* eigenmodes of the polarization data, the probability to exceed (PTE) the measured χ^2 for the sum of the various data splits ranges from 1.6×10^{-8} to 8.7×10^{-7}, while the χ^2 for the differences are found to be consistent with noise. The PTE for the χ^2 found for the total (that is, not split) high *s*/*n* polarization eigenmodes, corrected for the beam offset leakage, is 5.7×10^{-8}.

Likelihood analyses are in principle more model dependent, and the analyses reported make different assumptions for the shape of the polarization power spectrum. Using theory to select the angular scales on which DASI should be most sensitive, we calculate the likelihood for a flat bandpower in *E* and *B* over the multipole range $300 < l < 450$ and find that data are consistent with $B = 0$ over this range, but that $E = 0$ can be rejected with a PTE of 5.9×10^{-9}.

The choice of the model bandpower is more important when the full *l* range of the DASI data is analysed. In this case, the likelihood analyses indicate that a $l(l+1)C_l \propto l^2$ model for the *E*-mode spectrum is 60 times more likely than a $l(l+1)C_l =$ constant model. Further, a bandpass shape based on the concordance model is found to be 12,000 times more likely than the flat bandpower. The likelihood ratio test leads to a PTE of 8.5×10^{-7} for the concordance shaped bandpower, corresponding to a confidence of detection of 4.9σ. In all three of these tests, *B* is found to be consistent with zero, as expected in the concordance model.

The concordance model is also supported by the results of the five-band piecewise-flat analyses, *E*5/*B*5. The upper limit for the first *E* band at $28 \le l \le 245$ is only $2.38\,\mu\mathrm{K}^2$, a factor of 30 lower in power than the previous upper limit. The next band at $246 \le l \le 420$ is detected with a maximum likelihood value of $17.1\,\mu\mathrm{K}^2$. Such a sharp rise in power with increasing *l* is expected in the *E*-mode spectrum (see Fig. 4) owing to the length scale introduced by the mean free path to photon scattering. The polarization of the larger modes is suppressed because the velocity differences are not as large on the scale of the mean free path. In fact, the *E* spectrum is expected to increase as $l(l+1)C_l \propto l^2$ at small *l*. This dependence is not expected to continue to the higher *l* values to

which DASI is sensitive, owing to diffusion damping, which suppresses power on scales smaller than the mean free path. The maximum likelihood values of the higher l bands of the DASI five-band E analysis are consistent with the damped concordance model, but lie below a simple extrapolation of the l^2 power law. Again, the five-band B-mode spectrum is consistent with the concordance prediction of zero.

The TE analysis provides further confidence in our detection of CMB polarization and for the concordance model. From the $T/E/TE$ likelihood analysis, the $TE = 0$ hypothesis is rejected with a PTE of 0.054. Note that TE could be negative as well as positive and therefore the $TE \leq 0$ hypothesis is rejected with higher confidence.

Lastly, the measured T frequency spectral index, 0.01 (-0.16 to 0.14), is remarkably well constrained to be thermal and is inconsistent with any known foregrounds. The E frequency spectral index, 0.17 (-1.63 to 1.92), is also consistent with the CMB, and although less well constrained than the T index, is inconsistent with diffuse foreground synchrotron emission at nearly 2σ.

In summary, the analyses reported in this paper all indicate a robust detection of E-mode CMB polarization with a confidence level $\geq 4.9\sigma$. The measured properties of the polarization are in good agreement with predictions of the concordance model and, as discussed in the 'Foregrounds' subsection, are inconsistent with expectations from known sources of foreground emission. These results therefore provide strong support for the underlying theoretical framework for the generation of CMB anisotropy. They lend confidence to the values of the cosmological parameters and to the extraordinary picture of the origin and structure of the Universe derived from CMB measurements. The prospect of further refining our understanding of the Universe using precision polarization measurements is the goal of many ongoing and planned CMB experiments. The detection of polarization at the predicted level reported in this paper points to a promising future for the field. □

Received 7 October; accepted 5 November 2002; doi:10.1038/nature01269.

1. Penzias, A. A. & Wilson, R. W. A measurement of excess antenna temperature at 4080 Mc/s. *Astrophys. J.* **142,** 419–421 (1965).
2. Mather, J. C. *et al.* Measurement of the cosmic microwave background spectrum by the COBE FIRAS instrument. *Astrophys. J.* **420,** 439–444 (1994).
3. Fixsen, D. J. *et al.* The cosmic microwave background spectrum from the full COBE FIRAS data set. *Astrophys. J.* **473,** 576–587 (1996).
4. Smoot, G. F. *et al.* Structure in the COBE differential microwave radiometer first-year maps. *Astrophys. J.* **396,** L1–L5 (1992).
5. Miller, A. D. *et al.* A measurement of the angular power spectrum of the cosmic microwave background form l = 100 to 400. *Astrophys. J.* **524,** L1–L4 (1999).
6. Halverson, N. W. *et al.* Degree angular scale interferometer first results: A measurement of the cosmic microwave background angular power spectrum. *Astrophys. J.* **568,** 38–45 (2002).
7. Netterfield, C. B. *et al.* A measurement by BOOMERANG of multiple peaks in the angular power spectrum of the cosmic microwave background. *Astrophys. J.* **571,** 604–614 (2002).
8. Lee, A. T. *et al.* A high spatial resolution analysis of the MAXIMA-1 cosmic microwave background anisotropy data. *Astrophys. J.* **561,** L1–L5 (2001).
9. Pearson, T. J. *et al.* The anisotropy of the microwave background to l = 3500: Mosaic observations with the cosmic background imager. *Astrophys. J.* (submitted); preprint astro-ph/0205388 at ⟨http://xxx.lanl.gov⟩ (2002).
10. Scott, P. F. *et al.* First results from the Very Small Array - III. The CMB power spectrum. *Mon. Not. R. Astron. Soc.* (submitted); preprint astro-ph/0205380 at ⟨http://xxx.lanl.gov⟩ (2002).
11. Hu, W. & Dodelson, S. Cosmic microwave background anisotropies. *Annu. Rev. Astron. Astrophys.* **40,** 171–216 (2002).
12. Kaiser, N. Small-angle anisotropy of the microwave background radiation in the adiabatic theory. *Mon. Not. R. Astron. Soc.* **202,** 1169–1180 (1983).
13. Bond, J. R. & Efstathiou, G. Cosmic background radiation anisotropies in universes dominated by nonbaryonic dark matter. *Astrophys. J.* **285,** L45–L48 (1984).
14. Polnarev, A. G. Polarization and anisotropy induced in the microwave background by cosmological gravitational waves. *Sov. Astron.* **29,** 607–613 (1985).
15. Kamionkowski, M., Kosowsky, A. & Stebbins, A. Statistics of cosmic microwave background polarization. *Phys. Rev. D.* **55,** 7368–7388 (1997).
16. Zaldarriaga, M. & Seljak, U. All-sky analysis of polarization in the microwave background. *Phys. Rev. D.* **55,** 1830–1840 (1997).
17. Hu, W. & White, M. A CMB polarization primer. *New Astron.* **2,** 323–344 (1997).
18. Kosowsky, A. Introduction to microwave background polarization. *New Astron. Rev.* **43,** 157–168 (1999).
19. Hu, W., Spergel, D. N. & White, M. Distinguishing causal seeds from inflation. *Phys. Rev. D* **55,** 3288–3302 (1997).
20. Kinney, W. H. How to fool cosmic microwave background parameter estimation. *Phys. Rev. D* **63,** 43001 (2001).
21. Bucher, M., Moodley, K. & Turok, N. Constraining isocurvature perturbations with cosmic microwave background polarization. *Phys. Rev. Lett.* **87,** 191301 (2001).
22. Rees, M. J. Polarization and spectrum of the primeval radiation in an anisotropic universe. *Astrophys. J.* **153,** L1–L5 (1968).
23. Zaldarriaga, M. & Harari, D. D. Analytic approach to the polarization of the cosmic microwave background in flat and open universes. *Phys. Rev. D* **52,** 3276–3287 (1995).
24. Coulson, D., Crittenden, R. G. & Turok, N. G. Polarization and anisotropy of the microwave sky. *Phys. Rev. Lett.* **73,** 2390–2393 (1994).
25. Crittenden, R., Davis, R. L. & Steinhardt, P. J. Polarization of the microwave background due to primordial gravitational waves. *Astrophys. J.* **417,** L13–L16 (1993).
26. Seljak, U. Measuring polarization in the cosmic microwave background. *Astrophys. J.* **482,** 6–16 (1997).
27. Kamionkowski, M., Kosowsky, A. & Stebbins, A. A probe of primordial gravity waves and vorticity. *Phys. Rev. Lett.* **78,** 2058–2061 (1997).
28. Seljak, U. & Zaldarriaga, M. Signature of gravity waves in the polarization of the microwave background. *Phys. Rev. Lett.* **78,** 2054–2057 (1997).
29. Lyth, D. H. What would we learn by detecting a gravitational wave signal in the Cosmic Microwave Background anisotropy? *Phys. Rev. Lett.* **78,** 1861–1863 (1997).
30. Zaldarriaga, M. & Seljak, U. Gravitational lensing effect on cosmic microwave background polarization. *Phys. Rev. D* **58,** 23003 (1998).
31. Hu, W. & Okamoto, T. Mass reconstruction with cosmic microwave background polarization. *Astrophys. J.* **574,** 566–574 (2002).
32. Knox, L. & Song, Y. A limit on the detectability of the energy scale of inflation. *Phys. Rev. Lett.* **89,** 011303 (2002).
33. Kesden, M., Cooray, A. & Kamionkowski, M. Separation of gravitational-wave and cosmic-shear contributions to cosmic microwave background polarization. *Phys. Rev. Lett.* **89,** 011304 (2002).
34. Kamionkowski, M. & Kosowsky, A. The cosmic microwave background and particle physics. *Annu. Rev. Nucl. Part. Sci.* **49,** 77–123 (1999).
35. Staggs, S. T., Gunderson, J. O. & Church, S. E. *ASP Conf. Ser. 181, Microwave Foregrounds* (eds de Oliveira-Costa, A. & Tegmark, M.) 299–309 (Astronomical Society of the Pacific, San Francisco, 1999).
36. Caderni, N., Fabbri, R., Melchiorri, B., Melchiorri, F. & Natale, V. Polarization of the microwave background radiation. II. An infrared survey of the sky. *Phys. Rev. D* **17,** 1908–1918 (1978).
37. Nanos, G. P. Polarization of the blackbody radiation at 3.2 centimeters. *Astrophys. J.* **232,** 341–347 (1979).
38. Lubin, P. M. & Smoot, G. F. Search for linear polarization of the cosmic background radiation. *Phys. Rev. Lett.* **42,** 129–132 (1979).
39. Lubin, P. M. & Smoot, G. F. Polarization of the cosmic background radiation. *Astrophys. J.* **245,** 1–17 (1981).
40. Lubin, P., Melese, P. & Smoot, G. Linear and circular polarization of the cosmic background radiation. *Astrophys. J.* **273,** L51–L54 (1983).
41. Sironi, G. *et al.* A 33 GHZ polarimeter for observations of the cosmic microwave background. *New Astron.* **3,** 1–13 (1997).
42. Keating, B. G. *et al.* A limit on the large angular scale polarization of the cosmic microwave background. *Astrophys. J.* **560,** L1–L4 (2001).
43. Wollack, E. J., Jarosik, N. C., Netterfield, C. B., Page, L. A. & Wilkinson, D. A measurement of the anisotropy in the cosmic microwave background radiation at degree angular scales. *Astrophys. J.* **419,** L49–L52 (1993).
44. Hedman, M. M. *et al.* New limits on the polarized anisotropy of the cosmic microwave background at subdegree angular scales. *Astrophys. J.* **573,** L73–L76 (2002).
45. Cartwright, J. K. *et al.* Polarization observations with the cosmic background imager. in *Moriond Workshop 37, The Cosmological Model* (in the press).
46. de Oliveira-Costa, A. *et al.* First attempt at measuring the CMB cross-polarization. *Phys. Rev. D* (submitted); preprint astro-ph/0204021 at ⟨http://xxx.lanl.gov⟩ (2002).
47. Partridge, R. B., Richards, E. A., Fomalont, E. B., Kellermann, K. I. & Windhorst, R. A. Small-scale cosmic microwave background observations at 8.4 GHz. *Astrophys. J.* **483,** 38–50 (1997).
48. Subrahmanyan, R., Kesteven, M. J., Ekers, R. D., Sinclair, M. & Silk, J. An Australia telescope survey for CMB anisotropies. *Mon. Not. R. Astron. Soc.* **315,** 808–822 (2000).
49. Leitch, E. M. *et al.* Experiment design and first season observations with the degree angular scale interferometer. *Astrophys. J.* **568,** 28–37 (2002).
50. Pryke, C. *et al.* Cosmological parameter extraction from the first season of observations with the degree angular scale interferometer. *Astrophys. J.* **568,** 46–51 (2002).
51. Leitch, E. M. *et al.* Measurement of polarization with the Degree Angular Scale Interferometer. *Nature* **420,** 763–771 (2002).
52. Haslam, C. G. T. *et al.* A 408 MHz all-sky continuum survey. I—Observations at southern declinations and for the north polar region. *Astron. Astrophys.* **100,** 209–219 (1981).
53. Bond, J. R., Jaffe, A. H. & Knox, L. Estimating the power spectrum of the cosmic microwave background. *Phys. Rev. D* **57,** 2117–2137 (1998).
54. Seljak, U. & Zaldarriaga, M. A line-of-sight integration approach to cosmic microwave background anisotropies. *Astrophys. J.* **469,** 437–444 (1996).
55. White, M., Carlstrom, J. E., Dragovan, M. & Holzapfel, W. H. Interferometric observation of cosmic microwave background anisotropies. *Astrophys. J.* **514,** 12–24 (1999).
56. Hedman, M. M., Barkats, D., Gundersen, J. O., Staggs, S. T. & Winstein, B. A limit on the polarized anisotropy of the cosmic microwave background at subdegree angular scales. *Astrophys. J.* **548,** L111–L114 (2001).
57. Knox, L. Cosmic microwave background anisotropy window functions revisited. *Phys. Rev. D* **60,** 103516 (1999).
58. Halverson, N. W. *A Measurement of the Cosmic Microwave Background Angular Power Spectrum with DASI*. PhD thesis, Caltech (2002).
59. Tegmark, M. & de Oliveira-Costa, A. How to measure CMB polarization power spectra without losing information. *Phys. Rev. D* **64,** 063001 (2001).
60. Christensen, N., Meyer, R., Knox, L. & Luey, B. Bayesian methods for cosmological parameter estimation from cosmic microwave background measurements. *Class. Quant. Gravity* **18,** 2677–2688 (2001).
61. Wang, X., Tegmark, M. & Zaldarriaga, M. Is cosmology consistent? *Phys. Rev. D* **65,** 123001 (2002).
62. Wright, A. E., Griffith, M. R., Burke, B. F. & Ekers, R. D. The Parkes-MIT-NRAO (PMN) surveys. 2:

Source catalog for the southern survey ($-87.5° < \delta < -37°$). *Astrophys. J. Suppl.* **91,** 111–308 (1994).
63. Mason, B. S., Pearson, T. J., Readhead, A. C. S., Shepherd, M. C. & Sievers, J. L. The anisotropy of the microwave background to $l = 3500$: Deep field observations with the cosmic background imager. *Astrophys. J.* (submitted); preprint astro-ph/0205384 at ⟨http://xxx.lanl.gov⟩ (2002).
64. Zukowski, E. L. H., Kronberg, P. P., Forkert, T. & Wielebinski, R. Linear polarization measurements of extragalactic radio sources at λ6.3 cm. *Astron. Astrophys. Suppl.* **135,** 571–577 (1999).
65. Simard-Normandin, M., Kronberg, P. P. & Neidhoefer, J. Linear polarization observations of extragalactic radio sources at 2 cm and at 17-19 cm. *Astron. Astrophys. Suppl.* **43,** 19–22 (1981).
66. Simard-Normandin, M., Kronberg, P. P. & Button, S. The Faraday rotation measures of extragalactic radio sources. *Astrophys. J. Suppl.* **45,** 97–111 (1981).
67. Hildebrand, R. H. *et al.* A primer on far-infrared polarimetry. *Publ. Astron. Soc. Pacif.* **112,** 1215–1235 (2000).
68. Lazarian, A. & Prunet, S. *AIP Conf. Proc. 609, Astrophysical Polarized Backgrounds* (eds Cecchini, S., Cortiglioni, S., Sault, R. & Sbarra, C.) 32–43 (AIP, Melville, New York, 2002).
69. Tegmark, M., Eisenstein, D. J., Hu, W. & de Oliveria-Costa, A. Foregrounds and forecasts for the cosmic microwave background. *Astrophys. J.* **530,** 133–165 (2000).
70. Giardino, G. *et al.* Towards a model of full-sky Galactic synchrotron intensity and linear polarisation: A re-analysis of the Parkes data. *Astron. Astrophys.* **387,** 82–97 (2002).
71. Gaensler, B. M. *et al.* Radio polarization from the inner galaxy at arcminute resolution. *Astrophys. J.* **549,** 959–978 (2001).
72. Gray, A. D. *et al.* Radio polarimetric imaging of the interstellar medium: Magnetic field and diffuse ionized gas structure near the W3/W4/W5/HB 3 complex. *Astrophys. J.* **514,** 221–231 (1999).
73. Platania, P. *et al.* A determination of the spectral index of galactic synchrotron emission in the 1–10 GHz range. *Astrophys. J.* **505,** 473–483 (1998).
74. Banday, A. J. & Wolfendale, A. W. Fluctuations in the galactic synchrotron radiation—I. Implications for searches for fluctuations of cosmological origin. *Mon. Not. R. Astron. Soc.* **248,** 705–714 (1991).
75. Zaldarriaga, M. The nature of the E-B decomposition of CMB polarization. *Phys. Rev. D* (submitted); preprint astro-ph/0106174 at ⟨http://xxx.lanl.gov⟩ (2001).

Acknowledgements We are grateful for the efforts of B. Reddall and E. Sandberg, who wintered over at the National Science Foundation (NSF) Amundsen–Scott South Pole research station to keep DASI running smoothly. We are indebted to M. Dragovan for his role in making DASI a reality, and to the Caltech CBI team led by T. Readhead, in particular, to S. Padin, J. Cartwright, M. Shepherd and J. Yamasaki for the development of key hardware and software. We are indebted to the Center for Astrophysical Research in Antarctica (CARA), in particular to the CARA polar operations staff. We are grateful for contributions from K. Coble, A. Day, G. Drag, J. Kooi, E. LaRue, M. Loh, R. Lowenstein, S. Meyer, N. Odalen, R. Pernic, D. Pernic and E. Pernic, R. Spotz and M. Whitehead. We thank Raytheon Polar Services and the US Antarctic Program for their support of the DASI project. We have benefitted from many interactions with the Center for Cosmological Physics members and visitors. In particular, we gratefully acknowledge many conversations with W. Hu on CMB polarization and suggestions from S. Meyer, L. Page, M. Turner and B. Winstein on the presentation of these results. We thank L. Knox and A. Kosowsky for bringing the Markov technique to our attention. We thank the observatory staff of the Australia Telescope Compact Array, in particular B. Sault and R. Subrahmanyan, for providing point source observations of the DASI fields. This research was initially supported by the NSF under a cooperative agreement with CARA, a NSF Science and Technology Center. It is currently supported by an NSF-OPP grant. J.E.C. gratefully acknowledges support from the James S. McDonnell Foundation and the David and Lucile Packard Foundation. J.E.C. and C.P. gratefully acknowledge support from the Center for Cosmological Physics.

Competing interests statement The authors declare that they have no competing financial interests.

Correspondence and requests for materials should be addressed to J.M.K. (e-mail: john@hyde.uchicago.edu).

